Electroweak bubble wall expansion: gravitational waves and baryogenesis in Standard Model-like thermal plasma

Marek Lewicki, Marco Merchand and Mateusz Zych

Faculty of Physics, University of Warsaw,
ul. Pasteura 5, 02-093 Warsaw, Poland

E-mail: marek.lewicki@fuw.edu.pl, mmerchand@fuw.edu.pl,
mateusz.zych@fuw.edu.pl

ABSTRACT: Computing the properties of the bubble wall of a cosmological first order phase transition at electroweak scale is of paramount importance for the correct prediction of the baryon asymmetry of the universe and the spectrum of gravitational waves. By means of the semiclassical formalism we calculate the velocity and thickness of the wall using as theoretical framework the scalar singlet extension of the SM with a parity symmetry and the SM effective field theory supplemented by a dimension six operator. We use these solutions to carefully predict the baryon asymmetry and the gravitational wave signals. The singlet scenario can easily accommodate the observed asymmetry but these solutions do not lead to observable effects at future gravity wave experiments. In contrast the effective field theory fails at explaining the baryon abundance due to the strict constraints from electric dipole moment experiments, however, the strongest solutions we found fall within the sensitivity of the LISA experiment. We provide a simple analytical approximation for the wall velocity which only requires calculation of the strength and temperature of the transition and works reasonably well in all models tested. We find that generically the weak transitions where the fluid approximation can be used to calculate the wall velocity and verify baryogenesis produce signals too weak to be observed in future gravitational wave experiments. Thus, we infer that GW signals produced by simple SM extensions visible in future experiments are likely to only result from strong transitions described by detonations with highly relativistic wall velocities.

Contents

1 Introduction

The Standard Model (SM) of particle physics is one of the most successful theories ever devised. Although a plethora of experiments have verified the validity of the SM to high level of precision the SM is incapable to offer an explanation for the existence of dark matter, the baryon asymmetry of the universe (BAU) or the masses of neutrinos.

Cosmological first order phase transitions (FOPT) could be a vital ingredient in understanding the mechanism of dark matter production [1–4], account for the baryon asymmetry

of the universe [5–8] and be related to the origin of neutrino masses [9]. Additionally they could lead to an observable stochastic gravity wave (GW) background [10]. With recent detection of GWs from black hole mergers [11, 12] and hints of a stochastic background [13, 14] that could have been produced in the early Universe [15–24] this possibility has motivated many studies into probing various beyond the SM (BSM) scenarios predicting a FOPT through their GW signals [25–73] (for a comprehensive review see [74, 75]).

First order transitions are characterized by the nucleation of bubbles of a symmetry breaking vacuum phase [76–78] which subsequently expand and eventually collide ending the transition. Throughout the growth of the bubbles their spherical symmetry prohibits GW production. As the bubbles collide GWs can be sourced by the collisions themselves [79–84], however, this source is relevant only in strongly supercooled [81, 85] transitions in which plasma effects are suppressed. The source we will focus on comes from the motion of the plasma generated by its interactions with the bubble walls [86–92].

Between formation and collision, in a thermal plasma environment, the bubbles reach a steady state which is described by the velocity of the front interface and by the shape of its profile. Determination of these properties is crucial for making reliable predictions of the BAU and the GW spectrum. The first analytic formula, to the best of our knowledge, for the wall velocity was given by Andrei Linde in ref. [78]. Assuming non-relativistic walls $v \ll 1$, the plasma has a large heat conductivity and the bubble expansion is isothermal. There is an outward pressure given by the difference in energy density of the false vacuum to that in the true vacuum, i.e.,

$$\epsilon \equiv V(0, T) - V(\phi_0, T), \tag{1.1}$$

this is compensated by the extra pressure from particles that are reflected and accelerated after reaching the phase boundary. All particles that are massless in the false vacuum but obtain a mass $m \gg T$ cannot penetrate inside and gain energy after bouncing back into the space of false vacuum. Thus the extra pressure on the wall is

$$\Delta p = \left(\sum_i \frac{\pi^2}{30} g_i T^4 \right) v \tag{1.2}$$

where the sum is over all particles that become massive and g_i the number of degrees of freedom. From these equations one obtains

$$v = \frac{30\epsilon}{\sum_i \pi^2 g_i T^4}. \tag{1.3}$$

This simple picture is very intuitive and gives the right prediction, $v \to 0$ as $\epsilon \to 0$ as well as suggesting that lower temperatures produce faster walls which holds true generically. Another analytic estimate appeared in [93] where the authors used energy and momentum conservation across the wall and obtained instead the quadratic relation $v^2 \sim \Delta p/\Delta \rho$. It was assumed that the temperature and velocity across the wall are constant however we will show in the present paper that these changes cannot be brushed aside.

In ref. [94] it was shown that the analytic estimate of eq. (1.3) can only be applicable if the phase transition is strongly first order since in this case particles acquire a large

mass inside the bubble and are reflected off of the wall therefore damping its propagation. This case corresponds to the "thin-wall" approximation where the thickness of the wall is much smaller than all the other relevant length scales. Other important length scales to evaluate are the mean free paths for elastic scattering λ_{elastic} and for particle number changing processes $\lambda_{\text{inelastic}}$.

Three limiting situations were first identified in ref. [94] (see also [95]); (1) the thin-wall limit with $L_w < \lambda_{\text{elastic}}, \lambda_{\text{inelastic}}$, where L_w is the thickness of the wall and which corresponds to maximal departure from thermodynamic equilibrium, (2) the thick-wall case which is the opposite scenario with $\lambda_{\text{elastic}}, \lambda_{\text{inelastic}} < L_w$, in this case the particles that cross the wall have enough time to interact with the other particles in the plasma and thermal equilibrium is maintained and (3) the intermediate situation $\lambda_{\text{elastic}} < L_w < \lambda_{\text{inelastic}}$ where some approximate form of thermal equilibrium is expected.

The aforementioned results make clear that an estimation of the relevant hierarchy of length scales is pivotal for making a judicious choice of method for the computation of the wall properties. This, nonetheless, cannot be done a priori since the wall thickness is an unknown to begin with. For a given model the only thing one can do is to assume the propagation of the bubble falls into one of these limiting situations and to check the validity of the assumption a posteriori after applying a certain methodology.

Investigations of the wall properties assuming case (2), local equilibrium, include [64, 96–98] and in this case the only friction on the wall propagation comes from hydrodynamic effects of the plasma. On the other hand, if the wall is thin (but thicker than the particles thermal wavelength so that WKB approximation is valid), case (1), reflection and transmission of particles is appropriate to quantify the friction. Studies that fall into to this case can be found in [64, 65, 67, 99–101]. Recent methods aiming to compute the bubble wall velocity in strongly coupled theories using holography can be found in refs. [102, 103].

In the impractical scenario of a FOPT in the SM with a light Higgs mass, it has been found [94, 95] that the most likely limiting case is that of the intermediate region with a small departure from thermodynamic equilibrium, the case (3). One of the reasons being that in the SM we cannot ignore the effect of particles crossing the wall since some of the masses are comparable to the temperature. In ref. [95] it was found that the thin-wall scenario is unrealistic in the SM as it requires tuning the parameters of the theory. In this reference the authors showed that the typical mean free path of the heavier particles is of the same order as the width of the bubble wall and that a good approximation is to assume a small departure from local thermal equilibrium. In the same paper, as well as in [94, 104] it was recognized that in order to calculate the friction forces that stop the bubble wall requires solving the non-equilibrium distributions of the massive particles in the plasma. To do so one must solve a complicated system of Boltzmann transport equations. This was first performed in the electroweak theory in [95] and later in more detail by Moore and Prokopec in [105].

The method appropriate for case (3), henceforth called the *semiclassical* approximation [105], utilizes a three parameter *fluid* ansatz, which corresponds to perturbations in the chemical potential, temperature and velocity. The linear transport equations that follow are supplemented by the Higgs equation of motion (EOM) and a dynamical solution to the wall shape and velocity can be obtained.

The idea that the expansion of nucleated vacuum bubbles at finite temperature could correspond to the motion of detonation waves was first proposed by Steinhardt in ref. [106]. This was subsequently expanded [107] to include all possible solutions in which the bubble walls reach a constant finite velocity due to interactions with the plasma. The hydrodynamic effects governing friction were taken into account for the electroweak theory in [95, 108, 109].

The full inclusion of non-equilibrium particle populations, hydrodynamic effects as well as a leading order treatment (*leading-log* approximation) of all the relevant scattering and decay rates which enter the collision term was first undertaken in [110]. Here it was discovered that including the jump effect from hydrodynamics, the solutions become subsonic. Furthermore it was pointed out that their results underestimate the friction since the contribution from the Higgs self coupling and from infrared W bosons was ignored.

The semiclassical approximation has also been used for the singlet extension of the SM in refs. [111–113]. The inclusion of scattering processes that include the Higgs boson was done in ref. [112] and a calculation of the collision terms beyond *leading-log* was investigated in [72]. The effect of infrared gauge boson (also termed transition radiation) has been studied in [100, 101] and more recently in [67].

A simplified method of estimating the friction term in the Higgs EOM, called phenomenological approach has also been implemented in [109, 114–119]. This approach consists in adding a term $\propto \eta(v_w, \phi)u^\mu \partial_\mu$ to the Higgs EOM, where u^μ is the four velocity of the fluid and η is an ad-hoc parameter which can depend non-trivially on the wall velocity and on the Higgs field. It was shown in ref. [111] under which cases the phenomenological approach can reproduce all features of the Boltzmann equations.

In this paper we undertake the study of the wall expansion assuming the limiting situation (3) when there is a sizeable (but still small) departure from equilibrium. We base our calculations for the properties of the wall on the recently improved semiclassical fluid equations by Cline and Laurent [120]. Our primary focus here is to dissect the qualitative properties of the wall and their dependence on the parameters of the theory and how they correlate with the characteristics of the phase transition.

In order to remain consistent with current phenomenology of the SM while allowing for FOPTs we use as benchmark models the gauge singlet extension with parity symmetric potential and the SM effective field theory with a dimension six operator. While previous studies have focused [121] on the complementarity of GW signals with the BAU, here we build on these analyses by assessing the range of applicability of the semiclassical treatment and show that it is only limited to sufficiently weak transitions with transition strength parameter $\alpha \lesssim 0.1$. More precisely, we show that this approximation stops operating at the boundary between hybrid and detonation solutions. In other words, the Jouguet velocity marks the maximum speed of the bubble wall. Furthermore we draw a comparison with unsophisticated estimates for the wall velocity in the thin- and thick-wall approximations and we found remarkable agreement with the thick-wall formula. We provide a simple derivation for this formula and make a connection with recent results of wall velocities in thermal equilibrium [98]. A similar derivation for the wall thickness is carried out that gives a remarkably good approximation for the Higgs wall-thickness but overestimates the singlet thickness by a factor of about $\approx 7/5$ in all cases.

Using the benchmark models mentioned above we computed the BAU employing the updated transport equations of Cline and Kainulainen [122] and obtained the predictions for the spectrum of stochastic background of GWs comparing them with current and future sensitivities. We underscore the importance of doing the calculation with the correct variables in front of the wall as otherwise one would not obtain the correct baryon relic. We improve upon previous studies [121] by using two different BSM models which makes our qualitative results more general. We also computed the percolation temperature for the GW predictions which is usually a circumvented step.

The content of this paper is organized as follows: in section 2 we briefly review the formalism of bubble nucleation at finite temperature including percolation and present the most important parameters for GW spectrum. An overview of the hydrodynamic treatment of the plasma is presented in section 3. After that, in section 4, we review the improved transport equations and introduce the semiclassical approximation. Two separate subsections are devoted to show the most relevant improved fluid equations for the CP-even and CP-odd perturbations. We devote sections 5 and 6 to introduce the scalar singlet model and the SM effective field theory (SMEFT), respectively. Appropriate subsections in this section contain the results of the computations for the wall properties and for the BAU. The predictions for the GW spectrum are assembled together in section 7. In section 8 we discuss the comparison between our results and the thin- and the thick-wall approximations. A summary of this work and our conclusions are provided in section 9. We provide the formulas used in the finite temperature effective potential for the two benchmark models in appendices A and B.

2 Dynamics of the finite temperature phase transition

First-order phase transitions proceed via nucleation of bubbles of broken phase in the space filled with unstable phase. The probability of tunneling into the broken vacuum at temperature T is [78, 123]

$$\Gamma(T) = A(T)\mathrm{e}^{-S}, \tag{2.1}$$

where S is the Euclidean action of a critical bubble. For $O(3)$-symmetric thermal systems $S = \frac{S_3}{T}$. The prefactor $A(T)$ involves complicated functional determinants which are hard to compute. For tunneling at finite temperature it can be approximated as

$$A(T) = \left(\frac{S_3}{2\pi T}\right)^{\frac{3}{2}} T^4. \tag{2.2}$$

The nucleation temperature T_n is defined as the temperature at which the nucleation probability per horizon volume is of order 1. It corresponds to the condition

$$\int_{t_c}^{t_n} dt \frac{\Gamma(t)}{H(t)^3} = 1, \tag{2.3}$$

where t_c corresponds to the time at the critical temperature when both phases are degenerate and t_n the time when nucleation of bubbles begins. H denotes the Hubble rate which

in a radiation dominated epoch can be expressed as

$$H^2 = \frac{\rho_r}{3M_P^2}, \quad \rho_r \equiv \frac{\pi^2}{30}g_*(T)T^4, \tag{2.4}$$

where $M_P = 2.4 \times 10^{18}$ GeV is the reduced Planck mass and ρ_r the radiation energy density of relativistic species. To take into account the temperature dependence of the number of degrees of freedom $g_*(T)$, we use tabulated data from the estimates of ref. [124]. The nucleation condition (2.3) can also be approximately written as

$$\frac{S_3}{T_n} \approx 4\log\left(\frac{T_n}{H}\right), \tag{2.5}$$

which for temperatures around the electroweak scale gives us the approximate condition $S_3/T_n \approx 140$. This approximation is usually used in the literature for obtaining the nucleation temperature. For sufficiently strong transitions, however, this nucleation criteria has to be modified and in the most serious calculations one needs to include the vacuum contribution in the Hubble parameter and compute the temperature of percolation.

It is usually assumed, that first-order phase transitions are instant and complete at the temperature $T \approx T_n$. Therefore all the parameters determining gravitational-wave signal are typically evaluated at this value. However to be more accurate, one may consider a probability, that a randomly chosen point is still in the false vacuum, given by

$$P(t) = e^{-I(t)}, \tag{2.6}$$

where $I(t)$ corresponds to the fraction of the space which has already been converted to the broken phase, namely

$$I(t) = \frac{4\pi}{3}\int_{t_c}^t dt' \Gamma(t')a(t')^3 r(t,t')^3. \tag{2.7}$$

In the expression above, $r(t,t')$ denotes the comoving radius of a bubble nucleated at t' propagated until a subsequent time t and is given by

$$r(t,t') = \int_{t'}^t \frac{v_w(\tilde{t})d\tilde{t}}{a(\tilde{t})}, \tag{2.8}$$

with $a(t)$ the scale factor and $v_w(t)$ the wall velocity which, in principle, is time dependent.

In practical calculations, it is more convenient to use temperature T instead of time variable t and (2.7) takes the form

$$I(T) = \frac{4\pi}{3}\int_T^{T_c} \frac{dT'}{H(T')}\Gamma(T')\frac{r(T,T')^3}{T'^4}. \tag{2.9}$$

It is usually assumed that the transition completes when $P(t) \approx 0.7$, which leads to a percolation temperature T_p given by the following condition

$$I(T_p) = 0.34. \tag{2.10}$$

Although the percolation time provides a more accurate estimate of when the transition completes and one should in general evaluate all physical observables at this time, its calculation presents a serious challenge given the fact that the comoving radius in (2.8) depends on the velocity of the wall which is what we are aiming to achieve in this paper. A complete solution would require an iterative method which we consider a next level of diligence and we will leave this issue as beyond the scope of this paper.

Due to this complication our estimation for the wall velocity will be performed at the nucleation temperature, obtained from the condition $S_3/T_n \approx 140$. Then the value of v_w is used in eq. (2.8) to obtain the percolation temperature which we used for evaluating the GW spectrum.

Another approximation which has been used to assess the viability of electroweak baryogenesis (EWBG) is the evaluation of the sphaleron shutting off condition after the plasma enters inside the bubble. This has become known as the sphaleron washout condition [125] which translates into[1]

$$\frac{v_n}{T_n} \gtrsim 1.0, \tag{2.11}$$

with the numerical factor on the right hand side being a matter of some debate which could lead to slight modification in the range $1.5 - 0.5$ [126–128]. In this work we will use the sphaleron washout condition only for studying the shape of the parameter space and we will show its correlation with the other parameters of the phase transition. For the BAU computation this condition is already integrated in the formula for the final asymmetry.

To conclude this section we present the parameters which are relevant for the computation of the GW spectrum. The strength of the phase transition which, following [75],we define as

$$\alpha \equiv \frac{1}{\rho_r} \left(\Delta V_{\text{eff}}(\phi, T) - \frac{T}{4} \Delta \frac{\partial V_{\text{eff}}(\phi, T)}{\partial T} \right), \tag{2.12}$$

where the Δ symbol meaning the difference between the false vacuum value and that in the true vacuum. In the above formula we write a generic ϕ dependence on the potential but it should be clear that it actually means dependence from all scalar fields according to the BSM model. Additionally, the factor of $1/4$ in the second term on α above has been ommitted in past literature. We believe that it should be included, i.e. the strength is identified with the difference of the normalized trace of the energy momentum tensor as opposed to just the difference in the normalized energy density.

The other important parameter is the inverse time duration of the phase transition which is calculated as

$$\frac{\beta}{H} \equiv T_p \frac{d}{dT} \left(\frac{S_3}{T} \right) \Big|_{T=T_p}. \tag{2.13}$$

The parameters β and α introduced above and the bubble wall-velocity play a central role in determining the GW spectrum which will be discussed in a subsequent section.

---

[1]In the presence of extra scalars charged under $\text{SU}(2)_L$ this condition should be modified.

3 Hydrodynamic treatment

When computing the dynamic properties of the bubble wall and the BAU it is of crucial importance to take into account the hydrodynamic equations which model the plasma behavior [129]. These hydrodynamic equations, as written in the universe frame,[2] are given by [107]

$$(\xi - v)\frac{\partial_\xi e}{w} = 2\frac{v}{\xi} + [1 - \gamma^2 v(\xi - v)]\partial_\xi v\,,$$
$$(1 - v\xi)\frac{\partial_\xi p}{w} = \gamma^2(\xi - v)\partial_\xi v. \tag{3.1}$$

where e is the energy density, p the pressure and ω the enthalpy of the plasma. The variable $\xi = r/t$ accounts for the self-similarity of the equations and has units of velocity. For example $v(\xi_w)$ is the fluid velocity at the location of the bubble wall and $\xi_w = v_w$ is the wall velocity.

From these equations one can also obtain a differential equation for the temperature, simply by using the following identity

$$\frac{\partial p}{\partial T} = \partial_\xi p \frac{\partial \xi}{\partial T}, \tag{3.2}$$

from which it follows that the enthalpy can be written as

$$\omega \equiv T\frac{\partial p}{\partial T} = T\partial_\xi p\,(\partial_\xi T)^{-1}\,,, \tag{3.3}$$

and then pluggig into (3.1) one obtains

$$\frac{\partial_\xi T}{T} = \gamma^2 \mu \partial_\xi v, \quad \mu(\xi, v) = \frac{\xi - v}{1 - \xi v}. \tag{3.4}$$

The derivatives $\partial_\xi e$ and $\partial_\xi p$ can be related through the speed of sound in the plasma, $c_s^2 \equiv (dp/dT)/(de/dT)$, so as to get the central equation describing the velocity profile:

$$2\frac{v}{\xi} = \gamma^2(1 - v\xi)\left[\frac{\mu^2}{c_s^2} - 1\right]\partial_\xi v. \tag{3.5}$$

The hydrodynamic fluid equations are supplemented by boundary conditions on both sides of the wall which follow from the conservation of the energy momentum tensor accross the interface, namely

$$v_+ v_- = \frac{p_+ - p_-}{e_+ - e_-}\,, \quad \frac{v_+}{v_-} = \frac{e_- + p_+}{e_+ + p_-}, \tag{3.6}$$

with $+(-)$ meaning in front (behind) of the bubble wall. These conditions are derived in the rest frame of the bubble wall. It is important to keep track of which reference frame one is referring to in order to obtain consistent solutions. For the calculation of the BAU and the wall velocity one is interested in the thermodynamic properties of the plasma directly

---

[2]By universe frame we mean a reference frame far away from the wall, either inside or outside.

in front of the wall, i.e. v_+, T_+, α_+ etc. Failure to use the correct variables lead to no solution for the bubble wall velocity [121] and a significant underestimate for the BAU.

It is usually assumed that the system is well modeled by the bag equation of state which yields a relation between the plasma velocities [107]

$$v_+ = \frac{1}{1+\alpha}\left[\left(\frac{v_-}{2}+\frac{1}{6v_-}\right) \pm \sqrt{\left(\frac{v_-}{2}+\frac{1}{6v_-}\right)^2 + \alpha^2 + \frac{2}{3}\alpha - \frac{1}{3}}\right] . \qquad (3.7)$$

All the possible solutions to the hydrodynamic fluid equations have been classified in [107] and there are three possibilities: 1) Deflagration solutions have a subsonic wall velocity and are preceded by a shock front discontinuity which allows the solution to go to zero. The velocity of the plasma behind the wall vanishes, i.e. $v_- = v_w$. This type of solution lives in the lower branch of the above formula. 2) Detonations correspond to the opposite case with a vanishing velocity of the plasma in front of the wall and one has $v_+ = v_w$. In this case the solution is located in the upper branch of eq. (3.7) 3) Hybrid solutions are mixtures of the latter two and the velocity of the plasma is not vanishing on both sides of the wall. The thermodynamic variables in front of the wall, i.e. v_+, T_+ and α_+ are trivially found in the case of detonations. The cases of pure deflagrations and the deflagration component of hybrids however require some more work and in the remaining part of this section we summarize our procedure for them.

We show the temperature change across the wall for a given strength of the transition $\alpha = 0.05$ for three different wall velocities realised by the three solutions discussed above in figure 1. The key feature of deflagrations and hybrids is that the plasma is heated and accelerated in front of the bubble wall. As the velocity increases for a given strength of the transition, the fluid shell around it becomes steeper and thinner. The velocity at which the shell disappears altogether and we switch to a detonation solution is given by the Jouguet velocity [86, 106, 107]

$$v_J = \frac{1}{\sqrt{3}}\frac{1+\sqrt{3\alpha^2+2\alpha}}{1+\alpha} . \qquad (3.8)$$

This expression can be obtained from (3.7) by taking the limit $v_- = 1/\sqrt{3}$. This quantity will be of key importance to us because if the friction does not cease the wall acceleration before this velocity the surrounding temperature drops from T_+ to T_N . This further decreases the friction and makes finding solutions with larger velocities not possible via the semiclassical method.

3.1 Deflagrations

This type of solution is characterized by a subsonic bubble, i.e $v_w < c_s$ where v_w is the bubble wall velocity and c_s is the speed of sound in the plasma. A basic picture of this configuration is shown in figure 2.

One of the consequences of a deflagration solution is the appearance of a shock front which forms in front of the bubble wall interface and causes thermodynamic quantities to suffer discontinuities. Thus one has to deal with two interface boundaries which serve as two independent inertial reference frames. The velocity of the fluid as measured in these
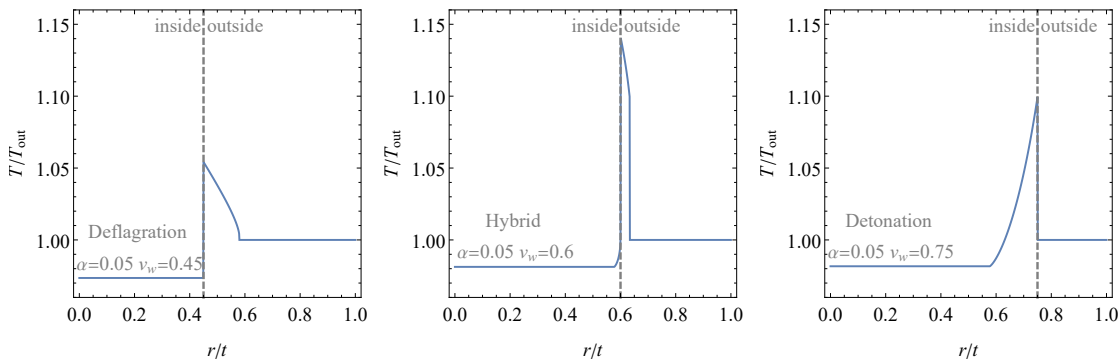
Figure 1. Temperature variation across the bubble wall for a transition with fixed strength $\alpha = 0.05$. The three panels correspond to $v_w = 0.45$, $v_w = 0.6$ and $v_w = 0.75$ and three different kinds of solution corresponding to a deflagration, a hybrid and a detonation.
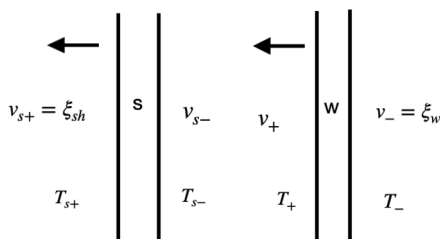

Figure 2. Diagrammatic picture for a deflagration bubble (w) propagating to the left as indicated by the arrows as well as the shock front (s) propagating in front of it. The fluid velocities and temperatures measured with respect to each wall interface are also indicated.

reference frames is therefore different depending on wether the fluid is in front or behind the interface. We will denote the fluid velocities as measured with respect to the wall (shock front) frame as v_+ (v_{s+}) if the fluid is in front and as v_- (v_{s-}) if the fluid is behind the front. See figure 2 for reference.

The wall and shock front discontinuities give rise to relations between the fluid velocities. Here we summarize them again for convenience. Across the bubble wall we have

$$v_+ v_- = \frac{p_+ - p_-}{e_+ - e_-}, \quad \frac{v_+}{v_-} = \frac{e_- + p_+}{e_+ + p_-}, \tag{3.9}$$

while for the shock front, since the fluid on both sides of it is actually in the symmetric phase of the theory, they are more simply written by

$$v_{s+} v_{s-} = \frac{1}{3}, \quad \frac{v_{s+}}{v_{s-}} = \frac{T_{s+}^4 + 3T_{s-}^4}{T_{s-}^4 + 3T_{s+}^4}. \tag{3.10}$$

Here it is useful to pause a moment to present a notation which was introduced in [112] to denote the fluid velocities as measured with respect to the center of the wall. Let us denote with $v_\pm$ ($v_{s\pm}$) the fluid velocities in the wall (shock front) frame while we will use tildes $\tilde{v}_\pm$ to refer to fluid velocities in the fluid reference frame. This has also been called the "frame of the universe" in refs. [118] (and more recently in [130]) in which the fluid

far ahead and behind of the bubble wall and shock front is at rest. Therefore the universe frame might also refer to a region of spacetime far ahead of the shock front where the fluid velocity vanishes. Here whenever we mention the universe frame we will simply mean the reference frame of the center of the bubble.

The fluid velocities in both frames are related by Lorentz transformations, i.e.

$$\tilde{v}_\pm = \frac{v_w - v_\pm}{1 - v_w v_\pm}, \quad \tilde{v}_{s\pm} = \frac{v_{sh} - v_{s\pm}}{1 - v_w v_{s\pm}}, \tag{3.11}$$

where v_w and v_{sh} are the relative velocities between the wall and shock front and the center of the bubble, respectively.

Now we can give a more precise definition of a deflagration. In this case the fluid velocity behind the wall is zero, i.e,

$$\tilde{v}_- = 0 \quad \longrightarrow \quad v_w = v_-. \tag{3.12}$$

Similarly the necessity of having a shock front is that we require that the fluid velocity jumps to zero in front of it. So we get

$$\tilde{v}_{s+} = 0 \quad \longrightarrow \quad v_{sh} = v_{s+}. \tag{3.13}$$

Since we are interested in the fluid velocity and temperature directly in front of the wall we need to solve their corresponding hydrodynamic equations

$$2\frac{v}{\xi} = \gamma^2 (1 - v\xi) \left[\frac{\mu^2}{c_s^2} - 1 \right] \partial_\xi v, \tag{3.14}$$

$$\frac{\partial_\xi T}{T} = \gamma^2 \mu \partial_\xi v \,. \tag{3.15}$$

Given α and some value for the wall velocity $v_w < c_s$, the boundary condition on the velocity equation is

$$\tilde{v}_+ \equiv \frac{\xi_w - v_+}{1 - \xi_w v_+} = v(\xi_w), \tag{3.16}$$

with $\xi_w = v_w = v_-$ the wall velocity and v_+ is determined by eq. (3.7) with the minus sign in front of the radical as is the case for deflagrations. The form of eq. (3.14) does not accept analytic solutions and a standard numerical integration would stop at the singular point $\mu^2 = c_s^2$. However the solution actually stops before reaching the singularity and the final point determines the velocity of the shock front which satisfies the relation:

$$\tilde{v}_{s-} \equiv \frac{\xi_s - v_{s-}}{1 - \xi_s v_{s-}} = v(\xi_s) \tag{3.17}$$

with $\xi_s = v_{sh} = v_{s+}$ the position of the shock front. Notice that the equation above has two unknowns, namely ξ_s and v_{s-}. This relation can be supplemented with the jump in velocities at the shock front eq. (3.10) as follows

$$v_{s-} = \frac{\xi_s - v(\xi_s)}{1 - \xi_s v(\xi_s)} = \frac{1}{3\xi_s}, \quad \rightarrow \quad \mu(\xi_s, v(\xi_s))\xi_s = \frac{1}{3} = c_s^2 \quad \text{(shock front position)}, \tag{3.18}$$

where on the left we Lorentz transformed (3.17) in favor of v_{s-}. Having solved for the velocity profile, the fluid velocities behind and in front of the wall and the shock front are completely specified. To determine the corresponding temperatures one needs to solve the equation for the temperature profile, eq. (3.15). One plugs in the solution $v(\xi)$ into the temperature equation and integrate. The boundary conditions relate the values of the temperature outside the wall T_+ with the temperature inside the shockfront T_{s-}. In reality what is fixed is their ratio, i.e.

$$\frac{T_+}{T_{s-}} = \exp\left[\int_{v_w}^{v_{sh}} d\xi \gamma^2 \mu \partial_\xi v\right] = \exp\left[\int_{\xi_w}^{\xi_{\text{shock}}} d\xi \frac{2c_s^2 v(\xi - v)}{\xi\left((\xi - v)^2 - c_s^2(1 - v\xi)^2\right)}\right]. \tag{3.19}$$

In addition one has to satisfy the boundary conditions at the shock front eq. (3.10). From these one can eliminate v_{s+} to find

$$\frac{T_{s-}^4}{T_N^4} = \frac{3(1 - v_{s-}^2)}{9v_{s-}^2 - 1}, \tag{3.20}$$

where we notice that the temperature in the region in front of the shock front corresponds to the nucleation temperature of the transition, i.e. $T_{s+} = T_N$. Using (3.19) and (3.20) we can write

$$\frac{T_+}{T_N} = \left(\frac{3(1 - v_{s-}^2)}{9v_{s-}^2 - 1}\right)^{1/4} \exp\left[\int_{\xi_w}^{\xi_{\text{shock}}} d\xi \frac{2c_s^2 v(\xi - v)}{\xi\left((\xi - v)^2 - c_s^2(1 - v\xi)^2\right)}\right]. \tag{3.21}$$

Notice that in the region of integration in the above formula the latent heat is given by its value in front of the bubble wall, α_+ which is different from α_N that is calculated from the phase transition properties . To find the correct α_+ we iterate the above procedure for T_+ until the condition $\alpha_+ T_+^4 = \alpha_N T_N^4$ is satisfied. This is a good approximation for the bag equation of state with equal number of degrees of freedom on each side of the wall. Once α_+ is found, v_+ is fixed by [107]

$$v_+ = \frac{1}{1 + \alpha_+}\left[\left(\frac{v_-}{2} + \frac{1}{6v_-}\right) \pm \sqrt{\left(\frac{v_-}{2} + \frac{1}{6v_-}\right)^2 + \alpha_+^2 + \frac{2}{3}\alpha_+ - \frac{1}{3}}\right]. \tag{3.22}$$

3.2 Detonations

Detonations constitute the opposite case to deflagrations, namely the bubble wall is supersonic $v_w > c_s$ and the fluid velocity in front of the wall vanishes, i.e. $\tilde{v}_+ = 0$ which means $v_w = v_+$. That is, the wall velocity equals the fluid velocity in front of the wall. For the nucleation temperature and strength of the transition it also follows that $T_N = T_+$ and $\alpha_N = \alpha_+$. For our purposes this case represents the most trivial one in regard to the BAU and the wall velocity calculation. We briefly review this case for completeness.

The fluid velocity behind the wall can be obtained by inverting (3.7) in favor of v_-,

$$v_- = \frac{1 - 3\alpha + 3v_+^2(1 + \alpha) + \sqrt{-12v_+^2 + (1 - 3\alpha + 3v_+^2(1 + \alpha))^2}}{6v_+}, \tag{3.23}$$

where we took the plus sign in the radical by definition. Contrary to the case of deflagrations which do not require further thinking in applying formula (3.7) for finding the fluid velocity in front of the wall, for detonations the above formula hides a non trivial constraint on α and v_w; we must require that the velocity is positive and that the term inside the square root do not become negative. It can be proven that the necessary and sufficient condition that satisfy these constraints is given by

$$\alpha \leq \frac{(1-\sqrt{3}v_+)^2}{3(1-v_+^2)}, \quad \text{(consistency condition)}. \tag{3.24}$$

This equation can be interpreted as an upper bound for the transition strength given the wall velocity. However we find this explanation to be counter-intuitive given the pipeline structure of our calculations where we first find the strength of the transition and after that we calculate the wall velocity. Thus we prefer to express the last equation in a form that is most suitable for our motives. Using $v_+ = v_w$ we can write it as

$$0 \leq (v_w - v_J^+)(v_w - v_J^-), \quad v_J^\pm = \frac{1}{\sqrt{3}}\frac{1 \pm \sqrt{3\alpha^2 + 2\alpha}}{1+\alpha}, \tag{3.25}$$

and since $v_J^+ > v_J^-$ we thus see that the Jouguet velocity encountered at the beginning of this section, eq. (3.8) indicates the lower bound for the wall velocity for which detonations can be found. Within the range $c_s < v_w < v_J$ neither deflagrations nor detonations can be obtained. This is the range of velocities for hybrids which we discuss next.

3.3 Hybrids

Now we discuss the computation of the thermodynamic variables in front of the wall v_+, T_+, α_+ for the case of hybrid solutions. As their name suggests, this type of solution has features of both deflagrations and detonations. The wall velocity in this case is not identified with neither v_+ nor v_- and it falls within the range $c_s < v_w \leq v_J$, the reason they are also called supersonic deflagrations.

The hybrid case is therefore a superposition of a deflagration and a detonation. For the detonation part we need to fix $v_+ = v_J^-$ in order to satisfy the consistency condition in eq. (3.25), doing so automatically fixes $v_- = c_s$. The initial condition for this part is found by Lorentz transforming to the fluid rest frame, i.e. $v(\xi_w) = \mu(\xi_w, v_-)$, see eq. (3.4). The deflagration component is solved by fixing as initial condition the alternative Lorentz transformation, i.e. $v(\xi_w) = \mu(\xi_w, v_+)$. The total solution is found by patching these two.

To obtain the thermodynamic variables in front of the wall in the hybrid case we apply the same procedure explained in section 3.1 to iteratively solve for α_+, T_+ and v_+.

To conclude this section we show examples of all three types of solutions for different values of α in figure 3. The wall interface is located at the maximum of each curve. For reference we show in each figure the speed of sound and the Jouguet velocity as vertical dot-dashed and dashed lines respectively.
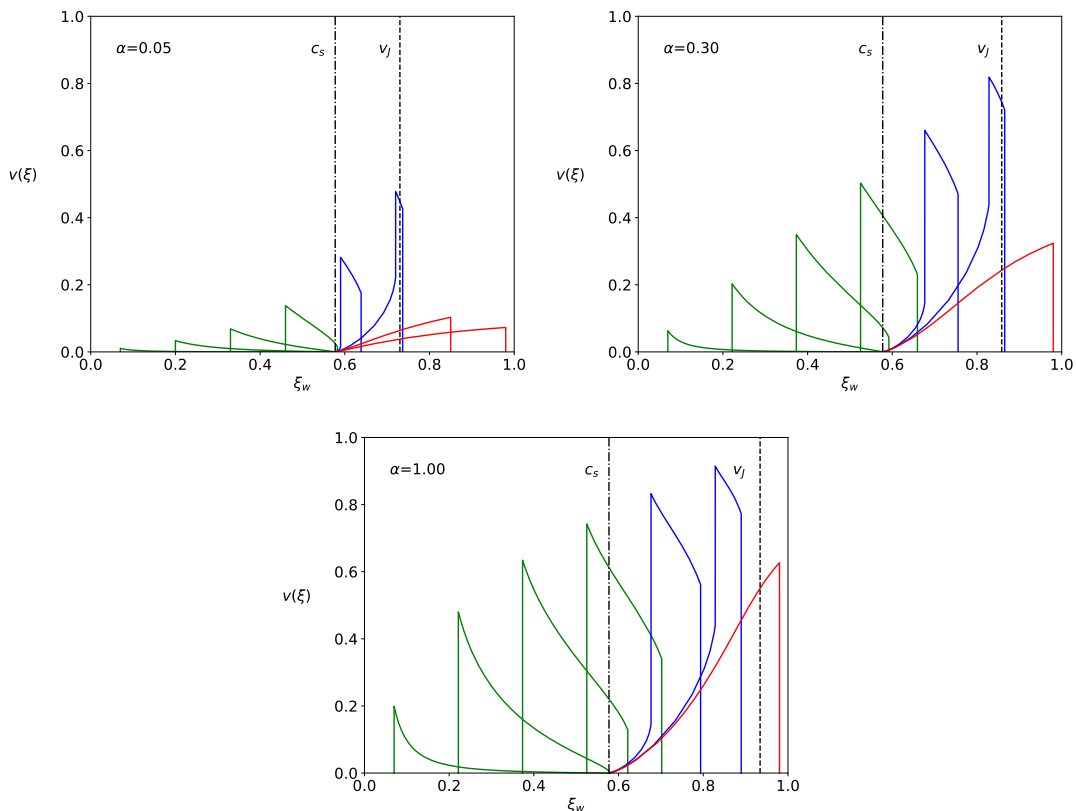
Figure 3. The hydrodynamics solutions for the velocity profile of the plasma around the bubble wall for $\alpha = 0.05$ in the upper left, $\alpha = 0.3$ in the upper right and $\alpha = 1$ in the bottom. Green curves are deflagrations, blue colored curves hybrids and red curves correspond to detonations.

4 Electroweak baryogenesis and bubble wall expansion

4.1 Review on updated transport equations

One of the most popular ways to account for the BAU is realised through EWBG, for a complete review see ref. [8]. In EWBG a first order phase transition is needed to provide the necessary out of equilibrium condition. The phase boundary exerts a force on the particles in the plasma perturbing their distribution functions from their equilibrium forms. Due to CP violation in the underlying theory, the form of this force depends on which particles it is acting upon, e.g. particles and anti-particles (as well as different helicity states) experience the same force but with opposite signs. Thus the effect of CP violation is to cause an asymmetry in the population densities of particles in front of the wall. This asymmetry biases the non-perturbative sphaleron rates to produce more baryons than anti-baryons. Then as the phase transition completes and the plasma is swept inside the bubble the sphaleron processes turn-off and the total baryon number freezes to its present value.

For quite some time it was commonly accepted that EWBG could only work if the bubble wall velocity is small $v \ll c_s$, with c_s the velocity of sound in the plasma, since otherwise the diffusion of the particle asymmetries would not be efficient. The claim [110],

that the wall velocity would have been subsonic in the SM, further motivated the derivation of the transport equations for particles asymmetries using the small velocity approximation $v \ll 1$. This approximation leads to transport equations which breakdown for wall velocities close to the speed of sound [131]. Recently, Cline and Kainulainen [122] have re-derived improved transport equations for arbitrary wall velocities arguing that the process of particle diffusion is not dependent on the propagation of sound waves in a plasma and thus even for highly relativistic walls one would expect a significant fraction of particles traveling faster than the wall and contributing to the diffusion tail. Using a scalar singlet model they showed that the baryon to entropy ratio is actually a continuous function of the wall velocity asymptotically reaching zero as $v \to 1$. Furthermore the transport equations are well behaved for velocities close to the speed of sound.

The Boltzmann transport equations for the out of equilibrium distribution functions can be separated into CP-even and CP-odd equations which can be solved independently of each other. While the CP-odd equations are suitable for computing the BAU, their CP-even counterparts can be used to predict the bubble wall velocity and its shape. These equations have also been improved for arbitrary wall velocities by Cline and Laurent in [120]. One crucial point of refs. [120, 122] has been to treat the velocity perturbations differently than the chemical potential and temperature fluctuations. In this case one does not assume a specific form for the velocity perturbation and instead uses a *factorization* assumption which allows one to factor out the velocity perturbation u from non-trivial integrals which appear when taking moments of the Liouville term. Also, in the case of the CP-odd equations, the authors used a *truncation* scheme which related higher moments of u to the first moment in a linear fashion.

As recognized in [120, 122], the factorization and truncation prescriptions, although leading to transport equations which do not breakdown for velocities close to the speed of sound, are somewhat arbitrary. Without these ad-hoc assumptions, it was shown [132] that the singularity at $v_w \approx c_s$ smooths out as one includes higher order terms in the momentum expansion, in coincidental agreement with the findings of [120]. More recently however, in ref. [133], it was argued that the un-physical singularity is in fact expected from hydrodynamics alone. The authors in [133] advocate for the use of a generalized fluid ansatz which corresponds to a higher order expansion and to the use of moments of the Boltzmann equations which follow from energy-momentum conservation. As of the time of writing of this paper, the formalism introduced in refs. [120, 122] has not been formally refuted nor confirmed thus the issue as to which set of equations capture the correct physics is still a matter of ongoing debate.

4.2 The semiclassical fluid approximation

In the semiclassical treatment as introduced in the seminal papers by Moore and Prokopec [105, 110] the Higgs EOM receives an extra contribution due to deviations from equilibrium in the particle distribution functions. This extra term is interpreted as a friction component and the distribution functions are calculated by means of Boltzmann equations.

The fluid approximation relies on the following assumptions: 1) that the deviations from equilibrium are small enough and the system of equations can be linearized, 2) the

time scale for the phase transition to complete is much smaller than the inverse Hubble rate and one is entitled to neglect the expansion of the universe which justifies the use of ordinary derivatives instead of the full covariant form of general relativity, 3) the de-Broglie thermal wavelength of particles in the system is smaller than the bubble wall thickness, this guarantees that the WKB approximation is valid for calculating the dispersion relations and group velocities. In addition we take it for granted that a steady state regime is achieved such that the wall has a well defined rest frame and furthermore that the bubble becomes sufficiently large for it to be treated as a planar surface.

In the following we will introduce the modified fluid equations as derived in [120, 122] for completeness. Starting from the Boltzmann equation which dictates the time evolution of the particle distribution of species a as

$$\frac{df_a}{dt} = \partial_t f_a + \dot{\vec{x}} \cdot \partial_{\vec{x}} f_a + \dot{\vec{p}} \cdot \partial_{\vec{p}} f_a = C[f_a], \tag{4.1}$$

where the dots denote time derivative. In the steady state the bubble has expanded sufficiently so that it can be viewed as a planar interface and the problem can be reduced to one dimension, the direction of the wall propagation . We work in the rest frame of the bubble wall where the first term on the left hand-side of the Boltzmann equation vanishes as the solution becomes static. The *fluid ansatz* for the distribution function is written as

$$f \approx f_v - f_v' \delta \bar{X} + \delta f_u + \mathcal{O}(\delta f^2), \tag{4.2}$$

with

$$f_v = \frac{1}{e^{\beta \gamma (E - v p_z)} \pm 1}, \quad f_v' \equiv \frac{df_v}{d\beta\gamma E}, \tag{4.3}$$

where this form makes manifest the Lorentz transformation to the wall frame and

$$\delta \bar{X} = \mu + \beta\gamma\delta\tau(E - v p_z), \tag{4.4}$$

encodes the perturbations from equilibrium. The variable μ is the chemical potential and $\delta\tau$ is the temperature perturbation. The extra term δf_u gives rise to the velocity perturbation and its form remains completely undetermined. The factorization prescription amounts to

$$\int d^3 p \ Q \ \delta f_u \rightarrow u \int d^3 p \ Q \ \frac{E}{p_z} f_v \tag{4.5}$$

for any prefactor Q that may appear when we take moments of the Boltzmann equation. As we mentioned above in the introduction, this prescription is arbitrary but it can be justified a posteriori by obtaining transport equations which are well behaved for all velocities.

The velocity and the force on the particle follow classical Hamiltonian equations of motion. For models where CP violation can be written as complex phases in fermionic mass terms, i.e., $m(z) = |m(z)|e^{i\gamma_5\theta(z)}$, the dispersion relation computed using the WKB approximation [134] gives

$$\dot{z} \equiv \frac{\partial\omega}{\partial p_z} = \frac{p_z}{E} + s\frac{m^2\theta'}{2E^2 E_z}, \qquad \dot{p_z} \equiv -\frac{\partial\omega}{\partial z} = -\frac{(m^2)'}{2E} + s\frac{(m^2\theta')'}{2E E_z}, \tag{4.6}$$

where primes denotes derivatives with respect to the transverse direction to the wall, ω is the energy of the WKB wave packet and $E_z^2 \equiv p_z^2 + m^2$. The variable $s = 0$ (1) for particles (anti-particles). In the derivation of the above equations an expansion in gradients ∂_z was assumed. Thus we see that CP violation appears at higher order in gradients and one can separate the Boltzmann equation as well as perturbations into CP even and CP odd components which can be independently solved. Solution to the CP even equations are connected to the bubble wall properties while the CP odd ones are useful for the computation of the BAU. In the following two subsections we present the most relevant formulas for each case.

4.2.1 CP-even equations: bubble wall properties

The derivation of the bubble wall properties entails solving the transport equations for the CP even perturbations. These can be obtained by inserting the force and group velocity of eq. (4.6) into the Boltzmann equation (4.1)

$$\left[\frac{p_z}{E} \partial_z - \frac{(m^2)'}{2E} \partial_{p_z} \right] \left(f_v - f_v' \delta \bar{X} + \delta f_u \right) = C[f],$$ (4.7)

where we used the fluid ansatz of eq. (4.2). Since this is a partial integro-differential equation with momentum and space-time dependence some form of massaging is necessary to obtain a tractable system of equations. First notice that in the fluid ansatz of eq. (4.2) three parameters were introduced, namely μ, $\delta\tau$ and u. Therefore it is customary to take moments of the Boltzmann equation for each variable that is introduced. The choice of weight factors for these moments is also somewhat arbitrary. In the improved fluid equations of [120] these were chosen as

$$\int d^3 p \frac{1}{T^3}, \quad \int d^3 p \frac{E}{T^4}, \quad \int d^3 p \frac{1}{T^3} \frac{p_z}{E}.$$ (4.8)

After some algebra and by grouping the perturbations in a vector object as $q = (\mu, \delta\tau, u)^T$ the simplified transport equations take the form

$$A_v \vec{q}\,' + \Gamma \vec{q} = S,$$ (4.9)

with

$$A_v = \begin{pmatrix} C_v^{1,1} & \gamma v C_0^{-1,0} & D_v^{0,0} \\ C_v^{0,1} & \gamma(C_v^{-1,1} - v C_v^{0,2}) & D_v^{-1,0} \\ C_v^{2,2} & \gamma(C_v^{1,2} - v C_v^{2,3}) & D_v^{1,1} \end{pmatrix},$$ (4.10)

and

$$S = \gamma v \frac{(m^2)'}{2T^2} \begin{pmatrix} C_v^{1,0} \\ C_v^{0,0} \\ C_v^{2,1} \end{pmatrix},$$ (4.11)

being the source term. The coefficients in the A matrix and in the source term are defined as non-trivial integrals of the particle distribution functions. They are given in equation (8) of [120]. The Γ matrix arises from treating the collision term and the numerical expressions

were recomputed in the *leading-log* approximation in the same reference. For more details we refer the reader to this reference.

In principle, the linearized transport equations presented above have to be solved for every particle in the plasma that is expected to contribute significantly to friction. For the SM extensions considered in this paper, the particles which contribute the most to the friction term are the heaviest SM particles, namely the top quark and the W and Z bosons. The remaining particles do not couple significantly to the Higgs and their interactions are assumed to be very efficient so that they equilibrate quickly and form a thermal background with a z dependent temperature and velocity. The effect of this background is taken into account by taking $\delta\tau \to \delta\tau + \delta\tau_{\text{bkgnd}}$, $u \to u + u_{\text{bkgnd}}$, where a z dependence on each term should be understood. This effect gives rise to additional transport equations for the background perturbations.

The Higgs EOM in the presence of out of equilibrium particle populations is given by [105, 110, 111, 135]

$$E_h \equiv \Box\phi + \frac{dV_{\text{eff}}(\phi, T)}{d\phi} + \sum_i \frac{dm_i^2}{d\phi} \int \frac{d^3p}{(2\pi)^3} \frac{\delta f_i(p, x)}{2E} = 0, \qquad (4.12)$$

where the sum in the last term is over all particles that receive mass from the Higgs condensate. This term is interpreted as a frictive force which must be carefully estimated for an accurate prediction of the bubble wall properties. Equations (4.9) and (4.12) form a consistent set of constraints for the out equilibrium particle distributions and for the Higgs condensate. In the presence of additional scalars, as in the case of extensions of the SM, one has to supplement this system with the corresponding equations of motion for each extra scalar. For the scalar singlet model considered in this paper one has to satisfy, in addition to (4.12),

$$E_s \equiv -s'' + \frac{\partial V_{\text{eff}}(h, s, T)}{\partial s} = 0, \qquad (4.13)$$

which doesn't have a frictive term because the singlet doesn't contribute to the Higgs mechanism of mass generation.

Calculation of the bubble wall velocity in the scalar singlet extension of the SM, see ref. [130], has shown that the scalar profiles can be well approximated by tanh functions. This form is well justified since the instanton solutions for bubble nucleation follow this shape so that scalar fields interpolate continuously across the bubble interface. Thus we use the expressions

$$h(z) = \frac{h_0}{2}\left[\tanh\left(\frac{z}{L_h}\right) + 1\right], \qquad (4.14)$$

$$s(z) = \frac{s_0}{2}\left[1 - \tanh\left(\frac{z}{L_s} - \delta_s\right)\right], \qquad (4.15)$$

with L_h, L_s denoting the bubble wall thicknesses and δ_s an extra off-set factor. The field values h_0 and s_0 do not necessarily correspond to the vevs obtained by the bubble nucleation calculation since the form of the bubble after it has reached a steady state

velocity is in principle different than its form during nucleation. We do expect however these latter values not to be too different in magnitude from the former.

By using the tanh ansatz in the field profiles one cannot expect that the EOMs to be satisfied everywhere in space. Instead one can impose that the EOM has two vanishing moments, i.e.

$$M_1 \equiv \int dz E_h h' dz = 0, \tag{4.16}$$

$$M_2 \equiv \int dz E_h h' [2h(z) - h_0] dz = 0. \tag{4.17}$$

The form of M_1 above has physical intuition as it corresponds to the total pressure acting on the wall. It must vanish for a steady state wall [105, 110]. The second condition[3] is interpreted as pressure gradients which mostly depend on the wall thickness.

To obtain the wall-velocity we follow the methodology introduced in [121]. Although this was introduced for the scalar singlet extension, it can however be applied to other (not very exotic) SM extensions as well. Here we summarize the workflow:

- For a given set of model parameters; m_s, λ_{hs} and λ_s we calculate the thermodynamic quantities of the nucleation process using the ComoTransitions code [136].

- Having the nucleation temperature T_N and the latent heat of the transition α_N we perform a grid scan in the v_w, L_h plane. At each point in this grid we perform the next steps:

  1. Solve the hydrodynamic equations for the energy budget of the FOPT, see section 3. This allows us to obtain the thermodynamic parameters evaluated in front of the wall, that is T_+, α_+, v_+.

  2. Modify the field amplitudes so that they satisfy the correct minimization conditions with the effective potential evaluated at the temperature in front of the wall, with

  $$\frac{dV_{\text{eff}}(h, 0, T_+)}{dh}\Big|_{h=h_0} = \frac{dV_{\text{eff}}(0, s, T_+)}{ds}\Big|_{s=s_0} = 0. \tag{4.18}$$

  3. Solve the transport equations (4.9) for the perturbations from equilibrium. This step determines the friction force in the Higgs EOM.

  4. Update the Higgs amplitude h_0 by requiring the Higgs EOM to be satisfied deep inside the bubble, that is

  $$\frac{\partial V_T(h, 0, T_+)}{\partial h}\Big|_{h=h0} + \sum_i \frac{dm_i^2}{dh} \int \frac{d^3 p}{(2\pi)^3} \frac{\delta f_i(p, z)}{2E}\Big|_{z \to \infty} = 0. \tag{4.19}$$

  5. Satisfy the singlet EOM by minimizing its action with respect to L_s and δ_s,

  $$S_{\text{scalar}} = \frac{s_0^2}{6L_s} + \int dz \left[V_{\text{eff}}(h, s, T_+) - V_{\text{eff}}(h, s^*, T_+) \right], \tag{4.20}$$

---

[3]This choice of M_2 differs from the one first introduced in refs. [105, 110] but we believe that the final solution for v_w should be only mildly dependent on which form of M_2 one adopts.
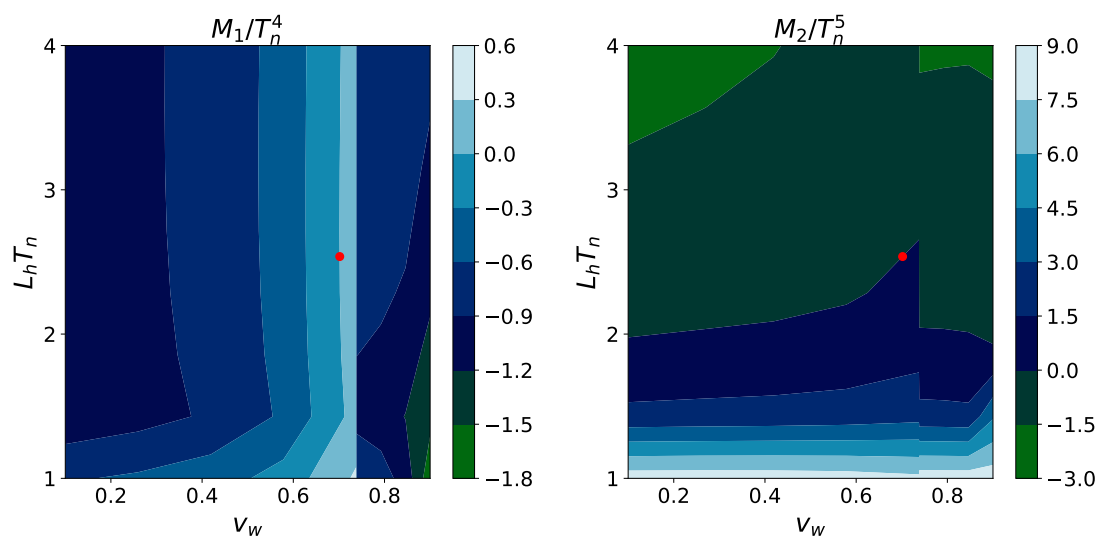
Figure 4. Moment grid for a model with $m_s = 80\,\text{GeV}$, $\lambda_{\text{hs}} = 0.84$ and $\lambda_{\text{s}} = 1$. The red point gives the minimum of the quadrature $f(v_w, L_h) = M_1^2 + M_2^2$.

where s^* is the scalar singlet profile with its parameters fixed as $L_s^* = L_h$ and $\delta_s^* = 0$.

6. Recompute the perturbations (4.9) and calculate M_1 and M_2.

The outcome of this algorithm for a single parameter space point is presented in figure 4 for a model with $m_s = 80\,\text{GeV}$, $\lambda_{\text{hs}} = 0.84$ and $\lambda_{\text{s}} = 1$. It shows filled contour plots with color maps for M_1 and M_2 normalized by appropriate factors of temperature. The red point on both plots shows the minimum of the scalar function $M_1^2 + M_2^2$.

The method of mapping the moments presented above is reliable in determining if there is a solution to eqs. (4.16) and (4.17). Unfortunately to obtain an acceptable level of precision it sometimes requires too many iterations which are time consuming. In order to achieve better precision one can use this mapping only to produce an initial guess for v_w and L_h and then feed this guess into a root finding algorithm.

4.2.2 CP-odd equations: BAU

As it has been mentioned in previous sections, the CP-odd contribution to the Boltzmann equations is what is needed to compute the BAU. In this subsection we present the simplified set of equations that one has to solve to achieve this goal. Here we only describe how the equations are obtained. For a full derivation we refer the reader to Cline and Kainulainen [122].

The starting point is (4.1) and now one includes in the group velocity and force the CP-violating contribution, i.e. the terms proportional to θ' in eqs. (4.6). At the same time the energy in the distribution function receives a CP-violating contribution of the form $E \to E - s\frac{m^2\theta'}{2EE_z}$, with $E \equiv \sqrt{\vec{p}^2 + m^2}$, the usual relativistic dispersion relation and $E_z \equiv \sqrt{p_z^2 + m^2}$. Since CP-violation is a higher order effect in an expansion in derivatives

we separate the chemical potential and the velocity perturbation in the following form

$$\mu \equiv \mu_e + s\mu_o,$$
$$\delta f \equiv \delta f_e + s\delta f_o, \tag{4.21}$$

with the subscript e (o) standing for even (odd). To obtain the CP-odd transport equations, moments from the Boltzmann equations were taken as follows

$$\frac{1}{N_1} \int d^3p, \qquad \frac{1}{N_1} \int d^3p \frac{p_z}{E}, \tag{4.22}$$

with $N_1 \equiv -\frac{2}{3}\pi^3 T^2 \gamma_w$. Additionally, for the BAU one does not need to include a temperature fluctuation and the linearized Boltzmann equations for a particle species take the form

$$Aw' + (m^2)'Bw = S + \delta C, \tag{4.23}$$

where $w = (\mu, u)^T$ and

$$A = \begin{pmatrix} -D_1 & 1 \\ -D_2 & R \end{pmatrix}, \quad B = \begin{pmatrix} -v_w\gamma_w Q_1 & 0 \\ -v_w\gamma_w Q_2 & \bar{R} \end{pmatrix}, \tag{4.24}$$

with coefficients that depend non-trivially on velocity and are given by integrals of the distribution function. The source terms $S_l = (S_1, S_2)^T$ are given by

$$S_{h\ell}^o = v_w\gamma_w s[(m^2\theta')'Q_\ell^{8o} - (m^2)'m^2\theta'Q_\ell^{9o}], \tag{4.25}$$

with non-trivial functions Q_ℓ^{8o} and Q_ℓ^{9o}. We notice that the derivation of the transport equations in [122] assumed that the wall is propagating from left to right. In this paper however we are considering the opposite case and we replace $v_w \to -v_w$.

The collision terms are generically given by

$$\delta C_1 = \sum_{ij} \Gamma_i s_{ij} \mu_j, \quad \delta C_2 = \Gamma_{\text{total}} u - v_w K_0 \delta C_1. \tag{4.26}$$

In the SM case we have

$$\delta\mathcal{C}_1^{t_L} = \Gamma_y(\mu_{t_L} - \mu_{t_R} + \mu_h) + \Gamma_m(\mu_{t_L} - \mu_{t_R}) + \Gamma_W(\mu_{t_L} - \mu_{b_L}) + \tilde{\Gamma}_{ss}[\mu_i],$$
$$\delta\mathcal{C}_1^{b_L} = \Gamma_y(\mu_{b_L} - \mu_{t_R} + \mu_h) + \Gamma_W(\mu_{b_L} - \mu_{t_L}) + \tilde{\Gamma}_{ss}[\mu_i],$$
$$\delta\mathcal{C}_1^{t_R} = -\Gamma_y(\mu_{t_L} + \mu_{b_L} - 2\mu_{t_R} + 2\mu_h) + \Gamma_m(\mu_{t_R} - \mu_{t_L}) - \tilde{\Gamma}_{ss}[\mu_i],$$
$$\delta\mathcal{C}_1^{h} = \Gamma_y(\mu_{t_L} + \mu_{b_L} - 2\mu_{t_R} + 2\mu_h) + \Gamma_h\mu_h, \tag{4.27}$$

with

$$\tilde{\Gamma}_{ss} = \Gamma_{ss}\left((1 + 9D_0^t)\mu_{t_L} + (1 + 9D_0^b)\mu_{b_L} - (1 - 9D_0^t)\mu_{t_R}\right). \tag{4.28}$$

In the above expressions $\Gamma_{\text{sph}} = 10^{-6}\,T$, $\Gamma_{ss} = 4.9 \times 10^{-4}\,T$, $\Gamma_y = 4.2 \times 10^{-3}\,T$, $\Gamma_m = \frac{m_t^2}{63\,T}$, $\Gamma_W = \Gamma_{h,\text{total}}$, $\Gamma_h = \frac{m_W^2}{50\,T}$ are the sphaleron, strong, top Yukawa, helicity-flips, W boson and Higgs number violation rates [137]. The total interaction rates are given in terms of diffusion constants, $\Gamma_{i,\text{total}} = D_2/(D_0\tilde{D}_i)$ with $\tilde{D}_h = 20/T$ and $\tilde{D}_q = 6/T$.

When studying the improved transport equations of Cline and Kainulainen [122] we noticed that there is a mismatch in mass dimensions between their equations (42) and (53); one needs to divide $\delta\bar{C}$ by $1/T$. To fix this mismatch we identified that their definition of the normalization factor K_0 given in their eq. (43) should carry an extra factor of $1/T$ as the same authors pointed out that $K_0 \cong 1.1$ for a massless fermion. On the other hand, for $v_w = 0.5$, it gives us $K_0 \cong 110$ without the extra factor of $1/T$ ($T = 100\,\mathrm{GeV}$ in their fiducial model). Additionally we believe there is a typo in their eq. (A5) for the helicity eigenstates, it should read

$$V = \frac{\tilde{p}_z^2}{\tilde{p}_z^2 + x^2} \frac{1}{\sqrt{1 - \frac{x^2}{\tilde{E}^2}}}. \tag{4.29}$$

We take into account these modifications throughout our calculations.

By solving the system (4.23) one obtains the total left-handed baryonic chemical potential

$$\mu_{B_L} = \frac{1}{2}(1 + 4D_0^t)\mu_{t_L} + \frac{1}{2}(1 + 4D_0^b)\mu_{b_L} + 2D_0^t\mu_{t_R}, \tag{4.30}$$

and the BAU can be calculated as [122]

$$\eta_B = \frac{405\,\Gamma_{\mathrm{sph}}}{4\pi^2 v_w \gamma_w g_* T} \int dz\, \mu_{B_{\mathrm{L}}} f_{\mathrm{sph}}\, e^{-45\Gamma_{\mathrm{sph}}|z|/4v_w}, \tag{4.31}$$

with $f_{\mathrm{sph}}(z) = \min(1, 2.4\frac{T}{\Gamma_{\mathrm{sph}}}e^{-40h(z)/T})$ introduced so that the integral interpolates smoothly the sphaleron contribution between false and true vacua.

5 The scalar singlet extension

It is known that in the SM the phase transition is a crossover and not suitable for explaining the BAU. Let us first consider the simplest extension of the SM which is the addition of an extra gauge singlet with a Z_2 symmetric potential, for other studies on this model see refs. [138–144].

5.1 Model notation and assumptions

The scalar potential at tree-level reads

$$V_0(\Phi, s) = -\mu_h^2 \Phi^\dagger\Phi + \lambda(\Phi^\dagger\Phi)^2 + \left(m_s^2 - \frac{\lambda_{hs}v^2}{2}\right)\frac{s^2}{2} + \frac{\lambda_s}{4}s^4 + \frac{\lambda_{hs}}{2}s^2\Phi^\dagger\Phi, \tag{5.1}$$

where $\Phi = (G^+, \frac{h+iG^0}{\sqrt{2}})^{\mathrm{T}}$ is the Higgs doublet with $v = 246$ GeV the SM Higgs vev. The mass squared term for the scalar singlet has been written in such a way that it is easy to see that m_s is the physical mass for the scalar singlet at the vacuum $(h, s) = (v, 0)$ which corresponds to the electroweak symmetry breaking (EWSB) vacuum.

We assume that at zero temperature the electroweak symmetry is broken by the vev of the Higgs doublet while the complex singlet does not develop a vev, see ref. [145], for a scenario that breaks the Z_2 spontaneously. As we will show below, the scalar singlet develops a vev at finite temperature and the Z_2 symmetry is broken at some point during

the thermal history. However we will assume, in the context of baryogenesis, that higher dimensional operators break the discrete symmetry explicitly and the occurrence of a domain wall problem is avoided. This explicit breaking also means that the singlet is not stable and doesn't contribute to the dark matter relic density at all. See refs. [36, 146] for analyses of this case.

Imposing the minimization conditions on the potential, namely that the first partial derivatives with respect to the fields vanish in the $(v, 0)$ vacuum, we obtain the familiar SM relation $\lambda = \frac{\mu_h^2}{v^2}$ and the Higgs mass is given by $m_h^2 = 2\mu_h^2$. Thus there are three free parameters coming from the tree-level scalar potential: m_s^2, λ_s and λ_{hs}.

We notice that the constraints imposed above are necessary conditions for the vacuum $(v, 0)$ to be a minimum of the tree-level potential. For some parameter values a second minimum in the s-field direction can develop, this situation corresponds to the case of $2m_s^2 < \lambda_{hs}v^2$ and this minimum might coexist with the EWSB minima. In this case one needs to check that the EWSB is indeed the global minimum.

The parameters of the tree-level potential are also constrained by the positivity requirement, i.e. that the potential doesn't become unbounded from below at large field values. Therefore one must have $\lambda > 0$ and $\lambda_s > 0$ and notice that if $\lambda_{hs} > 0$ the potential is automatically positive at large field values thus we only care about the case $\lambda_{hs} < 0$. A simple analytic analysis of the potential shows that the positivity requirement entails

$$\lambda_{hs} > -\sqrt{2\frac{m_h^2}{v^2}\lambda_s}. \tag{5.2}$$

Negative values of λ_{hs} do not lead to FOPTs and hence we will not consider this region of parameter space further in this paper. Another simplification that we will adopt in this work is to consider scalar singlet masses above the Higgs mass threshold, in other words we will only consider the case $m_s > 2m_h$ so that no exotic Higgs decays are predicted. This has been famously referred as the *nightmare* scenario in [143] because of its difficult prospects of detection at colliders. Moreover, since we are considering the case where the scalar singlet has vanishing vev at zero temperature, there is no eigenstate mixing between singlet and Higgs field and the two-loop Barr-Zee contributions to electron and neutron electric dipole moment (EDM) are absent.

The above simplifications allow us to put negligible focus on the collider constraints on this model, which have been studied elsewhere. Here we are primarily interested in calculating the bubble wall properties and their repercussions on the BAU and on the energy density of GWs.

To study the thermal history of the model one needs the one-loop Coleman-Weinberg contribution as well as the finite temperature potential for which we include the relevant formulas in the appendices. For the computation of the instanton solution of the Euclidean action we have made use of the publicly available CosmoTransitions code [136]. We modified the CosmoTransitions module for a generic potential to make it compatible with the on-shell renormalization prescription. Additionally we have written our own code with a simplified calculation that instead of calculating the trajectory in field space that minimizes the Euclidean action, uses overshooting along the path that minimizes the potential energy
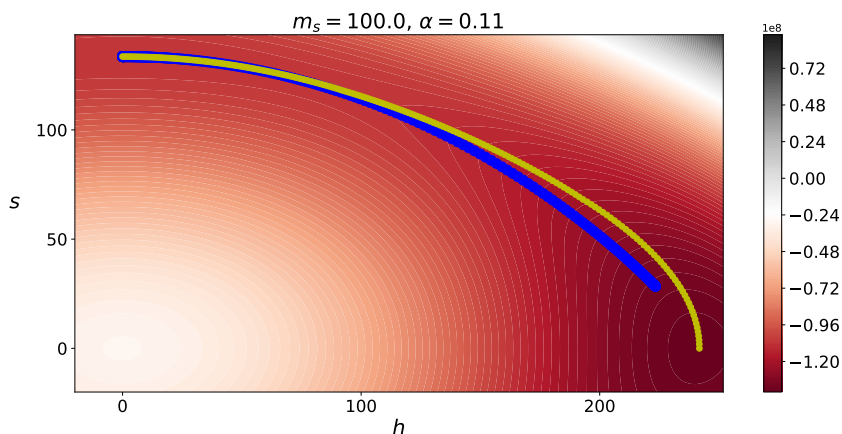
Figure 5. Contour plot of the effective potential for the scalar singlet model with parameters: $m_s = 100\,\text{GeV}$, $\lambda_{hs} = 0.93$, $\lambda_s = 1$. The blue dots represent the trajectory in field space of the instanton solution as obtained with CosmoTransitions while the yellow points show the path of minimum energy. The critical and nucleation temperatures are given by $T_c = 94\,\text{GeV}$ and $T_n = 59\,\text{GeV}$, respectively. These parameter space values yield a phase transition strength $\alpha = 0.11$.

(as in refs. [34, 147]). The EOM was solved for temperatures from the range in which two minima coexist. Sampling different values and checking the condition (2.5) at every step, we used a bisection algorithm to find the nucleation temperature. In a similar way, α and $\frac{\beta}{H}$ were evaluated. We cross-checked the output from the CosmoTransitions package with our own code and we found reasonably good agreement between the two methods.

An example of a parameter set that gives rise to a FOPT is presented in figure 5. This parameter space point exemplifies what is commonly called a two-step FOPT; at very high temperatures the only stable minimum of the effective potential lies at the origin of field space. Then as the universe evolves and the temperature drops a second minimum in the s field direction starts to form while the origin starts to become a local maximum. The transition in this case is second order. After more cooling the electroweak vacuum appears, eventually becoming degenerate with the s-vacuum. Afterwards the electroweak vacuum becomes the global minimum and a FOPT occurs at the nucleation temperature when the probability of bubble formation becomes comparable to the Hubble volume at that time.

On figure 5 we indicate the trajectory in field space as found by CosmoTransitions with the blue points while the yellow points show the path of minimum energy. One can easily observe a difference between the two paths in this case. While studying the parameter space of the model we noticed that for a given strength of the transition, bigger masses tend to deviate more from the minimum energy path. Furthermore, the range of FOPT strengths narrows down as the mass becomes smaller and the thin wall approximation becomes worse because the escape point is significantly far away from the global minimum around $(v, 0)$. This is why the blue points do no reach the other end in the figure. The parameter space point chosen in this case illustrate these two effects.

In this paper we will restrict our attention to two-step FOPTs as these type of transitions can provide CP violating mass terms for quarks at high temperature. In our case we
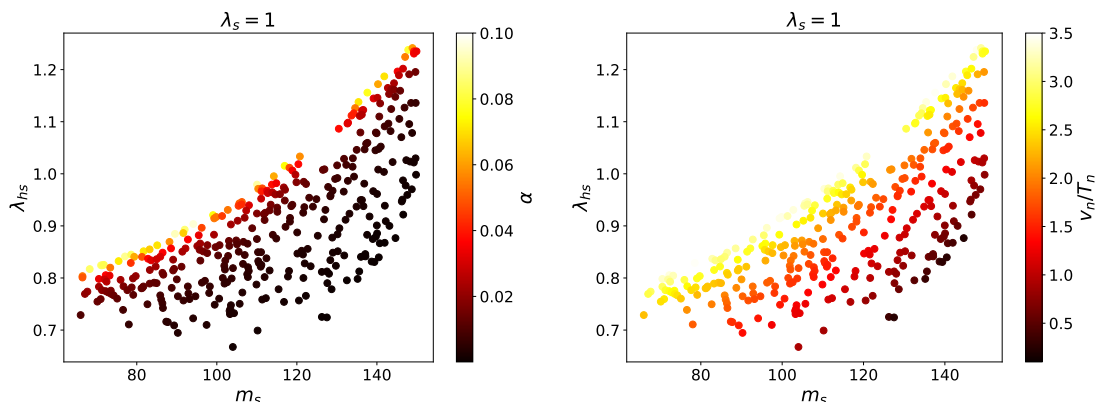
Figure 6. Parameter scan of the scalar singlet model featuring two-step FOPTs. *Left*: the color map indicates the value of the latent heat released during the transition. *Right* : the color shows the value of the sphaleron washout condition.

consider a complex mass term for the top quark via the following dimension-5 operator

$$\mathcal{L}_{\text{Yukawa}} \supseteq y_t \bar{Q} \Phi t_R \left(1 + \frac{is}{\Lambda_{\text{CP}}}\right) + \text{h.c.,} \tag{5.3}$$

where Λ_{CP} is some high energy cutoff scale and is treated as a free parameter. In principle one can also add similar operators for all SM fermions, however one expects their effect to be proportional to their Yukawa couplings which are suppressed relative to the top quark Yukawa coupling. We will ignore them completely in this paper. In the above expression we have set the Wilson coefficient of the dimension-5 operator equal to one imaginary unit. This is done for simplicity as it corresponds to maximal CP-violation.

We present, in figure 6, the result of a parameter scan of the scalar singlet model featuring two-step FOPTs with the singlet quartic coupling fixed to $\lambda_s = 1$ for simplicity. Changing the value of λ_s will not change the qualitative results and will only shift the points up or down. On the left, the color bar represents the latent heat released during the phase transition. This is also a measure of the strenght of the phase transition. The colorbar on the right shows the sphaleron washout condition.

The relevant "*arm*" of parameter space has a very well delineated structure: for a given mass, stronger transitions prefer larger values of the Higgs portal parameter. The same applies for the sphaleron condition. The white region (with no colored points) above the *arm* is excluded by the requirement of $(v, 0)$ to be the global minimum. The white region below the *arm* has too low values of λ_{hs} and there is no FOPTs there.

5.2 Bubble wall properties

As we have discussed in section 4.2.1, the bubble wall properties in the scalar singlet extension consist in the determination of the parameters v_w, L_h, L_s, h_0, s_0, δ_s which satisfy the set of equations (4.16), (4.17), (4.18), (4.19) and (4.20).

In order to produce easily readable results we choose four benchmark values for the scalar singlet mass $m_s = 70$, 80, 100, 120 GeV and we scan the Higgs portal parameter

λ_{hs} with values compatible with two-step FOPT. The singlet quartic coupling is set $\lambda_s = 1$ throughout the paper as we expect that varying its value will not have any qualitative repercussions on the results. This simplification has the added benefit that for a given mass the only micro-physical parameter from the Lagrangian is the Higgs portal coupling λ_{hs}. The value of this parameter then completely determines the properties of the FOPT and of the bubble wall. The results of the calculation are presented in figure 7. We show on the upper left plot the relation between the strength of the FOPT and the portal coupling. This is clearly the same pattern from figure 6 which indicates that stronger transitions are given by the largest possible value of λ_{hs}. On the upper-right the dimensionless wall thickness $L_h T_n$ is plotted against α, evidencing the inverse proportionality between the two. In the lower plots we show the dependence of the velocity on the strength (left) and on the wall thickness (right). These plots corroborate our intuition that: 1) stronger transitions lead to faster moving walls and 2) faster walls are thinner. It is important to mention that the lines of the plots in figure 7 terminate at some maximum value of the strength of the transition $\alpha_{\max}$. As we see in the lower left panel this corresponds to strong transitions for which the walls reach the Jouguet velocity (see eq. (3.8)). As we discussed in section 3, if the acceleration of the wall is not stopped by the friction below that velocity the solution changes into a detonation. As a result the heated plasma shell around the bubble disappears and the effective temperature determining the friction drops to the background temperature of the unbroken phase. This lowers the friction considerably and we never find solutions with $M_1 = M_2 = 0$ with higher velocities. This result agrees with [121] which also was not able to find the wall properties for detonation solutions for the same reason.

To conclude this section we explore the relationship between the rest of the bubble wall properties, namely the field amplitudes h_0, s_0, the scalar singlet thickness parameter L_s and the offset constant δ_s. These are shown in figure 8 for $m_s = 100\,\text{GeV}$. However, it is important to mention we have verified that the same qualitative behaviour follows for different masses. The two wall thicknesses are positively correlated as shown on the upper left plot with thicker walls requiring a bigger offset factor. This positive correlation was also reported in figure 7.c of ref. [121], however, due to the multiple parameter scan in that reference, it is hard to see the relation with the offset parameter. The field amplitudes h_0 and s_0 are also positively correlated and larger amplitudes are associated with faster walls. The plots on the bottom show the wall thicknesses L_h and L_s as function of h_0 and s_0, respectively. In both cases the larger the field amplitude the thinner the wall.

5.3 Baryogenesis

As a consequence of the higher dim-5 operator in (5.3) the top quark acquires a complex mass during the two-step FOPT. This mass term violates CP and is the source of the baryon assymmetry. The space-time dependent mass term in the Dirac equation of the top can be written as $m_t(z)e^{i\theta_t(z)}$, with

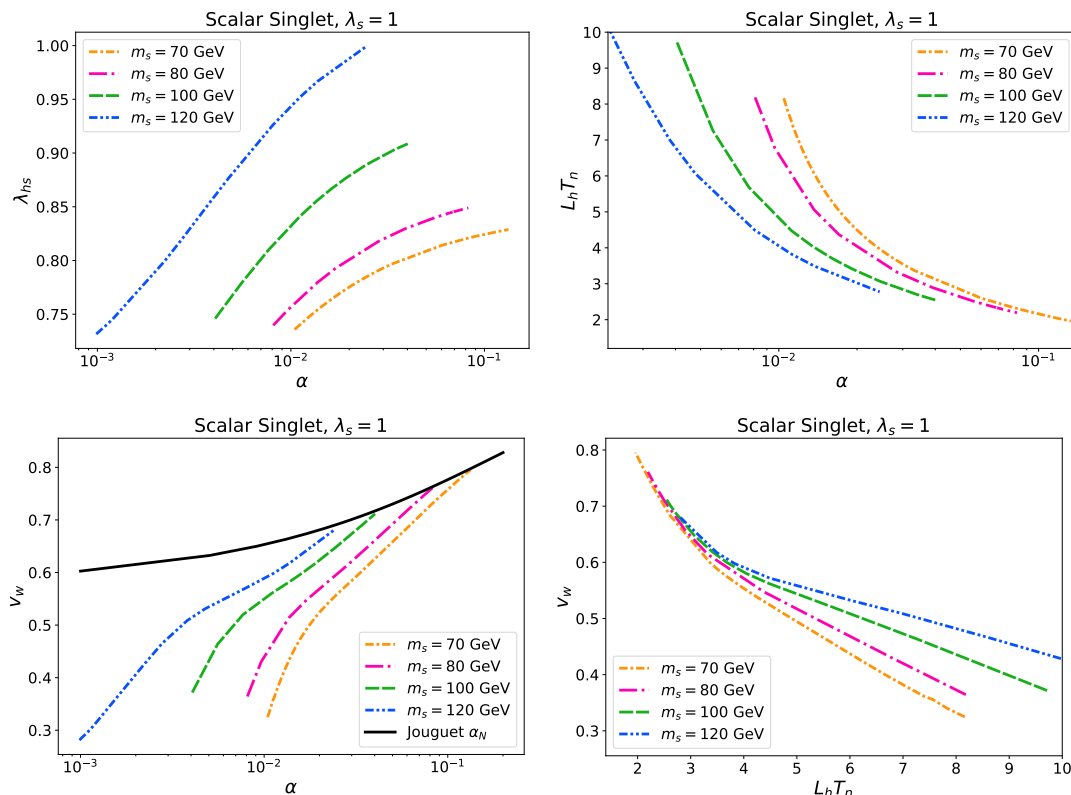$$m_t(z) \equiv \frac{y_t h(z)}{\sqrt{2}}\sqrt{1 + \frac{s(z)^2}{\Lambda_{\text{CP}}^2}}, \tag{5.4}$$

Figure 7. Results of the calculation for the bubble wall properties in the scalar singlet model for different m_s benchmarks. We have set $\lambda_s = 1$ everywhere and the qualitative description for each figure is provided in the text.

and the CP-violating phase

$$\theta_t(z) = \arctan\left[\frac{s(z)}{\Lambda_{\rm CP}}\right]. \tag{5.5}$$

We can see that the cutoff scale can affect the value of the top quark mass during the FOPT however we expect that this effect is not significant for the thermodynamic properties of the transition as well as the wall speed computation. Thus $\Lambda_{\rm CP}$ is taken as a free parameter which can be fixed to accommodate the final BAU.

In ref. [121] it was found that use of variables T_+ and v_+ including heating of the plasma around the bubble had a significant impact on computation of the wall properties. In this paper we emphasise this issue and show that this can also lead to considerable different estimates for the BAU. We illustrate this in figure 9 where we show the BAU, normalized to its observed value $\eta_{\rm obs} \approx 8 \times 10^{-11}$ [148, 149], computed using v_w, T_N in orange and with v_+ T_+ in blue. With the former variables one would conclude that the BAU yield decreases at higher wall velocities and none of the shown transitions can give the right amount of asymmetry. This is however not the case, as shown by the blue curves, the model with a velocity of about $v_w \approx 0.55$ (≈ 0.64) on the left (right) yields the right value of BAU. Therefore the inclusion of the hydrodynamic effects is key for correct baryogenesis predictions.
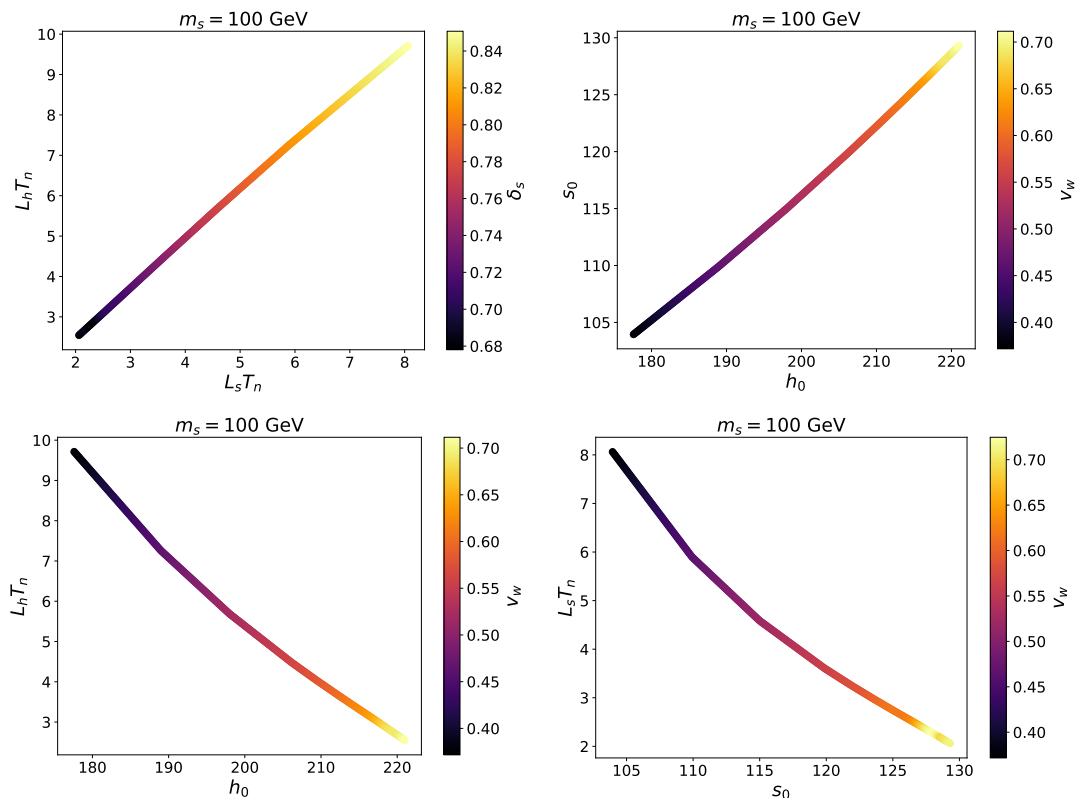
Figure 8. Correlation between parameters of the bubble wall. Color maps show the value of the offset parameter for the upper-left plot and the wall velocity for the rest of them. $\lambda_s = 1$ as in the rest of the paper.

The variation of the BAU with the cut-off scale can also be deduced from figure 9. For the cut-off values chosen one can directly observe the qualitative scaling $\eta_B \sim 1/\Lambda_{CP}$. Increasing the value of Λ_{CP} requires faster walls to explain the matter asymmetry. Furthermore the final BAU is well behaved for all the velocities computed which provides a consistency check of the possibility of baryogenesis for supersonic walls.

Figure 10 shows the cut-off scale Λ_{CP} necessary to obtain observed baryon asymmetry for our chosen range of masses $m_s = 70 - 120\,\text{GeV}$. According to [121], the value $\Lambda_{CP} \gtrsim 540\,\text{GeV}$ is consistent with experimental bounds on scalar singlet production at the LHC and agreeing with that reference we conclude it is not difficult to find plausible scenarios predicting the correct baryon asymmetry. Higher wall velocities (and stronger transitions) predict a larger asymmetry and the CP scale predicting the observed value can be as large as $\Lambda_{CP} \approx 1.5\,\text{TeV}$.

6 SMEFT

The SM effective field theory is a low energy representation of a possibly more UV completed theory. To parametrize our ignorance to the physics at high energy scales one adds a tower of higher dimensional operators that are consistent with the gauge symmetries of the
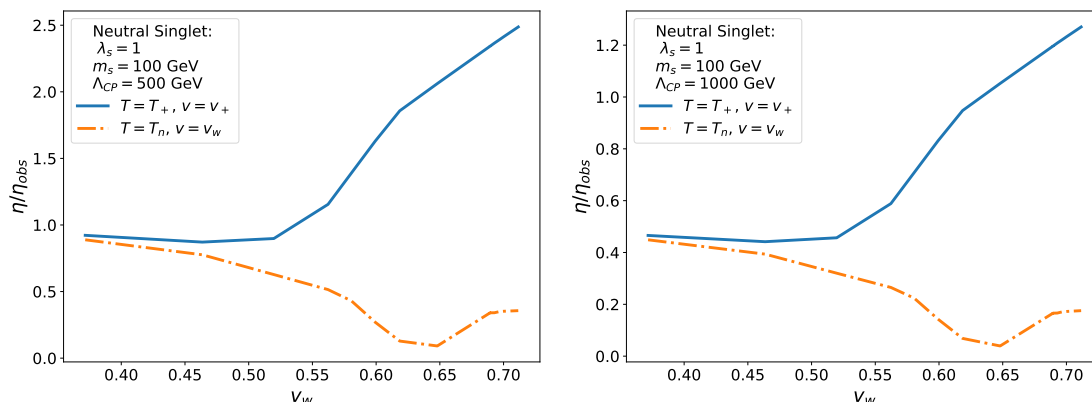
Figure 9. Prediction for the BAU normalized to its observed value in the scalar singlet model using the correct variables in front of the wall T_+, v_+ (blue solid) and using the naive variables T_n, v_w (orange dash-dot). The parameters have been fixed as indicated. The horizontal axis gives the wall velocity of each parameter set.
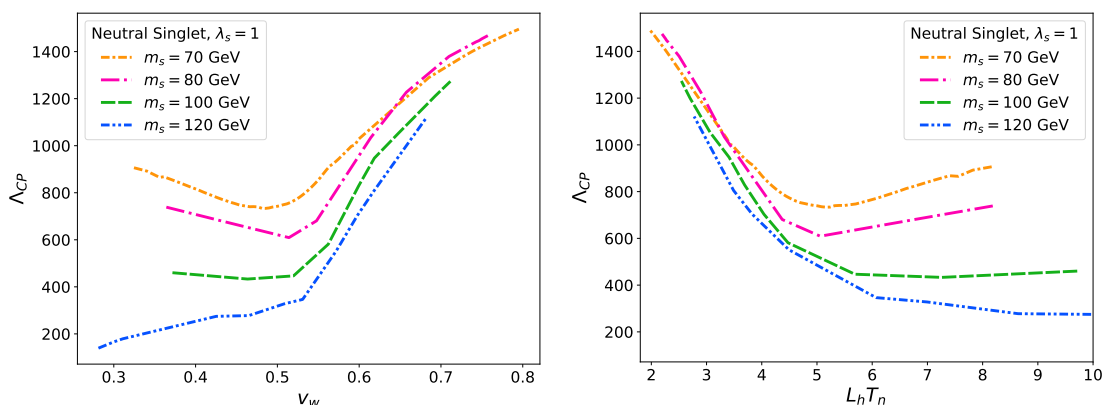

Figure 10. Cut-off scale $\Lambda_{\rm CP}$ required to obtain the observed baryon asymmetry as a function of the wall velocity (left panel) and wall thickness (right panel) in three benchmark values of the mass $m_s = 70, 80, 100, 120\,{\rm GeV}$ in the scalar singlet model.

SM and suppressed by a high energy scale Λ. In our case we consider the scalar potential augmented by a dimension six operator, namely

$$V_0 = -m^2 \Phi^\dagger \Phi + \lambda (\Phi^\dagger \Phi)^2 + \kappa (\Phi^\dagger \Phi)^3, \tag{6.1}$$

in this notation $\kappa \equiv 1/\Lambda^2$. The vacuum stability conditions at tree-level are

$$V'(h=v) = 0, \quad V''(h=v) = m_h^2, \tag{6.2}$$

which allow us to express the parameters in the potential as

$$m^2 = \frac{m_h^2}{2} - \frac{3v^4}{4\Lambda^2}, \quad \lambda = \frac{m_h^2}{2v^2} - \frac{3v^2}{2\Lambda^2}, \tag{6.3}$$

notice that for sufficiently low values of the cutoff scale, the quartic coupling can have negative values. This allows the formation of a tree-level potential barrier giving rise to FOPT.

The relevant formulas for the one-loop corrections and the temperature dependent masses are relegated to an appendix. It is also important to mention that including higher dimensional operators would not change the possible results for transition parameters instead simply mapping our one variable Λ onto a certain combination of more operators [41].

A comment about the use of the effective field theory should be provided; it has been shown [150] that the *projection* between the scalar singlet model (both with and without Z_2 symmetry) and SMEFT up to the dimension six operator in the potential is not always one-to-one with regards to the character of the phase transition. In other words, some regions of parameter space which show FOPT within the scalar singlet model do not always manifest the same type of transition when mapped onto the low energy effective field theory (EFT). The main problem lies on the fact that strongly FOPTs in the scalar singlet model are located in a region of parameter space with lower masses and large mixing quartic λ_{hs}. This is in direct tension with the premises of effective field theory which requires a large separation of scales (large masses in this case) so that heavy physics are sufficiently decoupled and the EFT remains valid.

The possibility of EWBG within the SMEFT has been scrutinized in ref. [151] where the authors directly tested one of the fundamental properties of effective field theories; the use of the EOM to remove redundant operators. This means operators that are related by the EOM should lead to the same physical prediction up to higher order effects in the perturbative EFT expansion. In that reference two different types of CP violating operators, connected by the EOM, were used to predict the EDM contributions and the BAU. While it was found that both operators give the same prediciton for the EDM, the prediction for the BAU was significantly different unless higher order effects are included. Their results thus contradict the hypothesis of EFTs about the redundancy of operators connected by the EOM in the context of EWBG. A very similar of study appeared in [152] by some of the same authors which further confirmed the breakdown of the EFT for the purposes of EWBG calculations. In this paper we do not interpret eq. (6.1) as coming from any particular UV completion and we treat it simply as a *toy* model for which we can compute the properties of the phase transition and apply the semiclassical treatment for the bubble wall velocity and the BAU.

6.1 Bubble wall properties

Calculating the wall velocity in SMEFT is relatively easier than with the scalar singlet scenario. In this case the grid scan method presented in section 4.2.1 has less steps since one only needs to satisfy the Higgs EOM. Furthermore in this model the cutoff scales Λ and Λ_{CP} are the only parameters that have to be fixed and they are disentangled with respect to the bubble wall properties and the BAU, respectively.[4]

The outcome of the computation of the bubble wall shape and speed is displayed in figure 11 which shows different cross sectional views of the velocity, thickness and amplitude as well as their dependence on Λ. The main qualitative results found for the scalar singlet

---

[4]The top quark field dependent mass in (6.5) has a direct dependence on Λ_{CP} and this might affect the calculation of the FOPT quantities. For the values of Λ_{CP} considered here we expect this effect to be negligible.
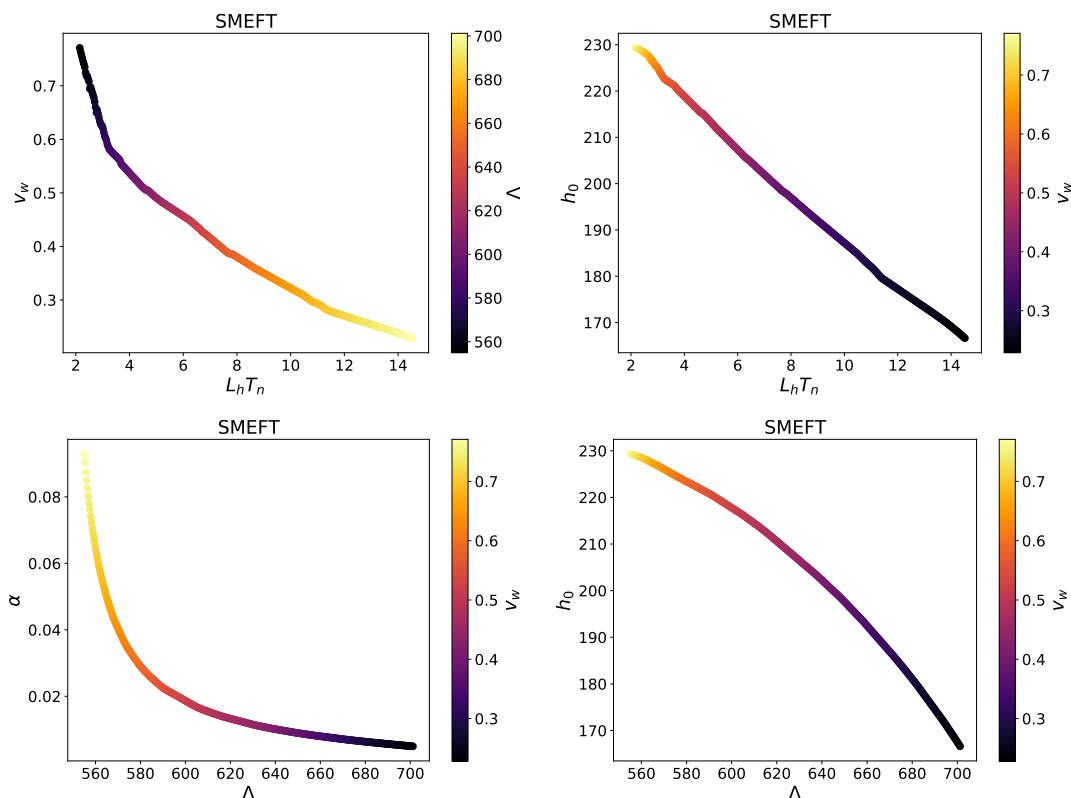
Figure 11. Bubble wall properties in the SMEFT. Color bar shows the value of Λ in the upper left figure and of v_w in the rest of them.

model also hold here; thicker walls are slower and larger field amplitudes correspond to faster walls, this is represented by the upper plots.

The cutoff Λ in the SMEFT completely determines the character of the FOPT with smaller values of Λ giving the strongest possible transitions. The points scanned for Λ terminate for low values because the $h = 0$ becomes the deepest minimum of the potential while for very high values one starts recovering the SM for which a FOPT is not possible.

6.2 Baryogenesis in SMEFT

In order to compute the BAU in this model we introduce CP violation in the following form

$$\mathcal{L}_{\text{Yukawa}} \supseteq y_t \bar{Q}\Phi t_R + \frac{y'}{\Lambda_{\text{CP}}^2}\bar{Q}\Phi t_R(\Phi^\dagger\Phi) + \text{h.c.} \tag{6.4}$$

where we assume the coefficient of the higher dimensional operator is purely complex $y' = i$, which corresponds to maximal CP violation. It is also assumed that the only CP violating operator is the one presented above. We also ignore the existence of other higher dimensional operators that might have phenomenological constraints. For a study of operators with constraints from precision electroweak observables see [153].
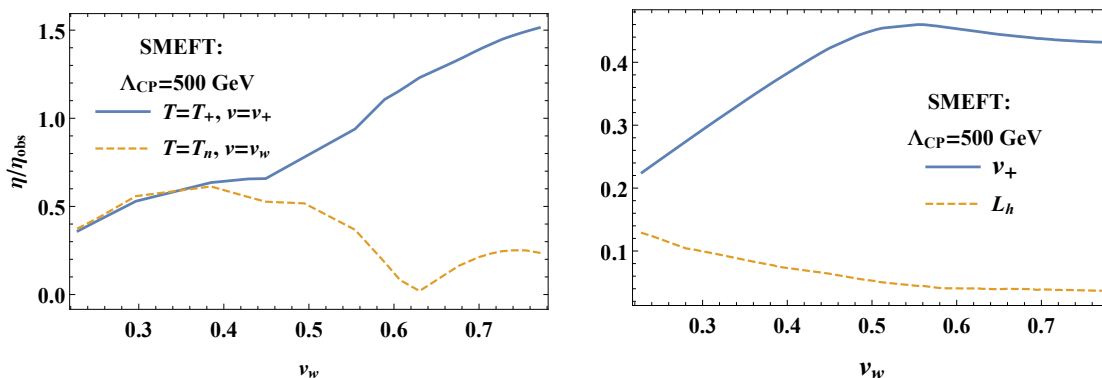
Figure 12. Left: normalized BAU against the wall velocity computed for the SMEFT. Right: the variation of the wall properties as function of velocity. The CP-violating cut-off scale was fixed to $\Lambda_{\mathrm{CP}} = 500\,\mathrm{GeV}$ in both cases.

As a consequence of (6.4), a space-time dependent complex mass term for the top quark appears, that is, $m_t(z)e^{i\theta_t(z)}$, with

$$m_t(z) \equiv \frac{y_t h(z)}{\sqrt{2}}\sqrt{1 + \frac{h(z)^4}{4\Lambda_{\mathrm{CP}}^4}}, \tag{6.5}$$

and the CP-violating phase

$$\theta_t(z) = \arctan\left[\frac{h(z)^2}{2\Lambda_{\mathrm{CP}}^2}\right]. \tag{6.6}$$

The WKB approximation for computing the BAU in SMEFT has been investigated in [154]. In this reference the authors considered the two thresholds to be correlated, i.e. $\Lambda = \Lambda_{\mathrm{CP}}$, and showed the observed BAU could be obtained. When this reference appeared the Higgs boson had not yet been discovered and the physical Higgs mass was taken as a free parameter. At the same time the authors examined the properties of the bubble wall using the analytic estimates of ref. [155]. The study of the bubble wall properties and EWBG within the SMEFT in this paper thus provides an updated and improved analysis compared to that reference. Moreover we consider the case of decoupled thresholds, i.e. $\Lambda \neq \Lambda_{\mathrm{CP}}$ as it has been shown in ref. [156] that the parameter space is ruled out for $\Lambda = \Lambda_{\mathrm{CP}}$ unless one includes extra CP-violating higher dimension operators to provide a cancellation for EDM contributions.

Figure 12 shows the baryon yield normalised to the observed value as a function of the wall velocity for fixed $\Lambda_{\mathrm{CP}} = 500\,\mathrm{GeV}$. We again highlight the impact of using the parameters T_+ and v_+ in front of the wall in comparison with the naive ones T_n and v_w. As we can see, for the latter case, the model can never produce the observed BAU. In the right hand side panel of figure 12 we show values of relevant parameters again as a function of the wall velocity. The only thing that varies in this plot is the cut-off scale of the dim-6 operator, all other quantities have been computed from first principles.

Figure 13 shows the cut-off scale Λ_{CP} necessary to produce the observed baryon asymmetry as a function of the cut-off scale in the scalar potential (left) and of the bubble thickness (right) in SMEFT. The colorbar shows the value of the wall velocity. One can
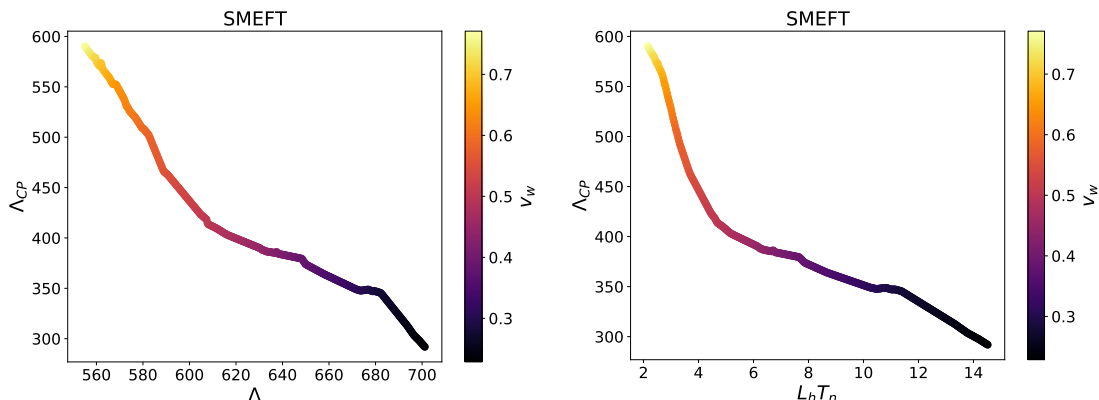
Figure 13. Cut-off scale $\Lambda_{\rm CP}$ necessary to produce the observed BAU as a function of the cut-off scale of the scalar potential (left) and of the bubble wall thickness (right) in SMEFT

see that the allowed scale for BAU has negative correlation with the cut-off scale in the scalar potential, i.e., smaller Λ values are associated with stronger phase transitions and faster walls pushing the scale $\Lambda_{\rm CP}$. The same result we found in the singlet model. At the same time, thicker walls yield the lowest $\Lambda_{\rm CP}$ necessary for the correct asymmetry.

Even though $\Lambda_{\rm CP}$ reaches only a few hundred GeV for the stronger transitions, the bound from EDM constraints on CP violating cutoff has been estimated to be in the multi TeV range, i.e., [152] $\Lambda_{\rm CP} > 2.5$ TeV and we conclude that SMEFT cannot be responsible for the baryon asymmetry unless some additional mechanism is added to hide the CP violating interactions from EDM experiments.

7 Gravitational wave signals

In this section we will discuss stochastic gravitational wave backgrounds produced by the first order phase transitions our models predict. Given the transitions in question are relatively weak and the walls never reach very relativistic velocities we will exclusively focus on GWs sourced by plasma motion [74, 75]. Thus we will neglect the bubble collision contribution which would necessarily require a much stronger transition [81, 82, 84, 157] not feasible in our models featuring polynomial potentials [90]. Further, despite recent progress concerning GWs produced by turbulence [158–160] the overall size of this contribution sourced by a phase transition remains uncertain and following [75] we will neglect it. Finally for the range of wall velocities we compute it seems crucial to use updated hybrid calculations of GW generation through sound waves in the plasma [88, 91, 161, 162] predicting a non-trivial dependence of the spectral shape on the wall velocity. However, we have checked these modifications have a negligible impact on the observational prospects of upcoming experiments simply because for weak signals these are dominated by the peak abundance which is not significantly modified.

As a result we will use the results of lattice simulations for the GW signal from sound waves [87, 89, 163] as summarised in [74, 75]. The abundance of the signal can be ex-

pressed as

$$\Omega_{\rm sw}(f)h^2 = 4.13 \times 10^{-7} \, (R_* H_*) \left(1 - \frac{1}{\sqrt{1 + 2\tau_{\rm sw}H_*}}\right) \left(\frac{\kappa_{\rm sw}\,\alpha}{1+\alpha}\right)^2 \left(\frac{100}{g_*}\right)^{\frac{1}{3}} S_{\rm sw}(f)\,, \quad (7.1)$$

$$S_{\rm sw}(f) = \left(\frac{f}{f_{\rm sw}}\right)^3 \left[\frac{4}{7} + \frac{3}{7}\left(\frac{f}{f_{\rm sw}}\right)^2\right]^{-\frac{7}{2}}\,, \quad (7.2)$$

with the peak frequency given by

$$f_{\rm sw} = 2.6 \times 10^{-5} {\rm Hz} \, (R_* H_*)^{-1} \left(\frac{T_p}{100 {\rm GeV}}\right) \left(\frac{g_*}{100}\right)^{\frac{1}{6}}\,. \quad (7.3)$$

where g_* is the number of degrees of freedom at temperature T_p for which we use the results of [124]. The duration of the sound wave period normalised to Hubble can be approximated as [81, 89, 90, 92, 164]

$$\tau_{\rm sw}H_* = \frac{H_* R_*}{U_f}\,, \quad U_f \approx \sqrt{\frac{3}{4}\frac{\alpha}{1+\alpha}\kappa_{\rm sw}}\,. \quad (7.4)$$

The average bubble radius normalised to Hubble rate can be approximated as

$$H_* R_* \approx (8\pi)^{\frac{1}{3}} \, {\rm Max}(v_w, c_s) \left(\frac{\beta}{H}\right)^{-1}\,, \quad (7.5)$$

using duration of the transition from eq. (2.13). Finally we calculate the sound wave efficiency factor κ_{sw} using the fluid profiles velocity and temperature profiles as explained in section 3. This quantity can be approximated as the energy converted into bulk fluid motion, given by [107]

$$\kappa_{sw} = \frac{3}{\alpha\,\rho_{\rm R}\,v_w^3} \int w\,\xi^2 \frac{v^2}{1-v^2} d\xi = \frac{4}{\alpha\,v_w^3} \int \left(\frac{T(\xi)}{T_p}\right)^4 \xi^2 \frac{v^2}{1-v^2} d\xi\,. \quad (7.6)$$

Figures 14 and 15 show GW spectra produced in the SMEFT and neutral singlet models together with power-law integrated sensitivity of LIGO [165–168] together with upcoming laser interferometer experiments LISA [169, 170] and ET [171, 172] as well as future devices based on atom interferometry [173] AEDGE [174] and AION-1km [175]. Figure 16 shows the corresponding signal to noise ratio for LISA and AEDGE. We find that only a very small fraction of the parameter space of SMEFT predicts a transition strong enough to be observed while in the scalar singlet model none of the transitions for which we can verify baryogenesis can be observed [121].

While both models are of course capable of supporting much stronger transitions with clearly visible signals [74, 75] we focus only on the cases in which friction of the plasma is large enough for the walls to cease accelerating below the Jouguet velocity. Only in those cases we are able to compute the wall velocity and width and calculate the final baryon yield, see figure 17. If the acceleration of the wall is not stopped below the Jouguet velocity we obtain a detonation solution in which plasma in front of the wall is no longer heated up. As a result above this threshold the friction on the wall drops significantly and we don't find any solutions until the fluid approximation breaks down at $v_w \approx 1$ rendering our calculation inadequate and viability of baryogenesis uncertain.
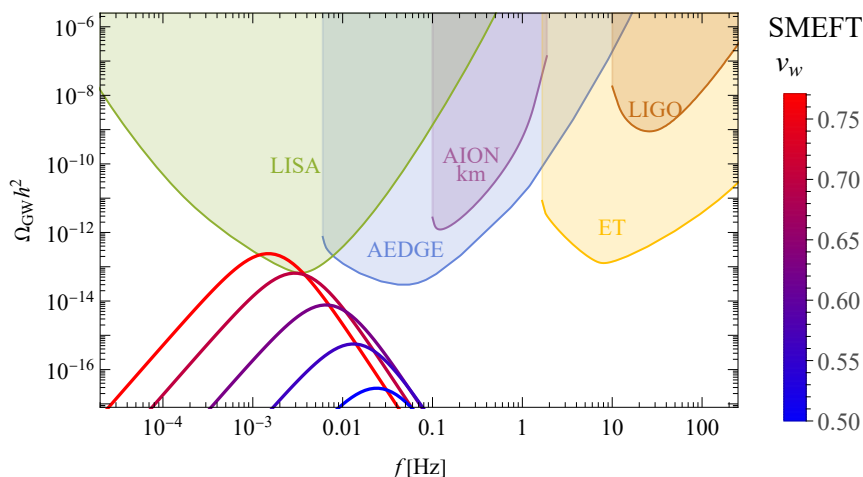
Figure 14. Gravitational wave signals for a range of parameters starting with the strongest transitions in the SMEFT model together with power-law integrated sensitivities of current and upcoming experiments.
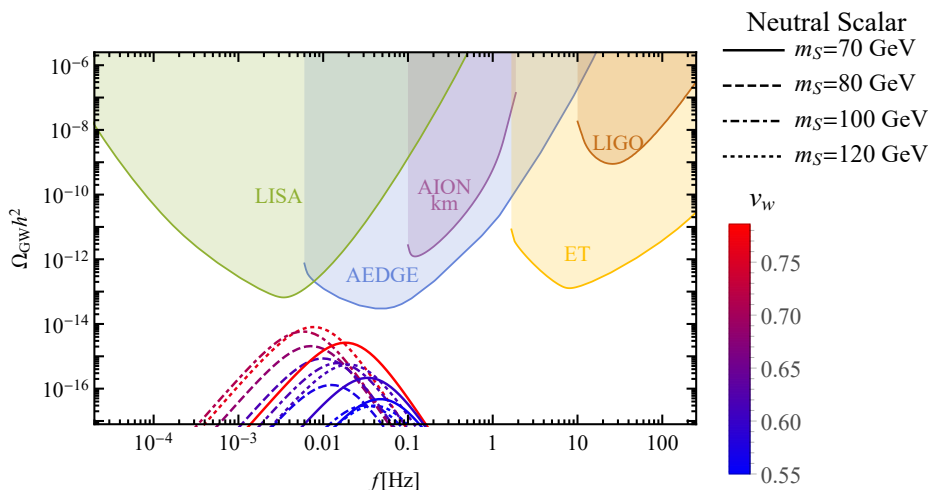

Figure 15. Gravitational wave signals for a range of parameters starting with the strongest transitions in the SM plus neutral scalar model together with power-law integrated sensitivities of current and upcoming experiments.

8 Simple estimate for the wall velocity and thickness

In this section we will discuss methods that can approximate the wall velocity in a simple manner. Starting with the thermal equilibrium formula [93] corrected for the cases in which the transition is too strong and the fluid approximation breaks down

$$
v_w = \begin{cases} \sqrt{\dfrac{\Delta V}{\alpha \rho_r}} & \text{for} \quad \sqrt{\dfrac{\Delta V}{\alpha \rho_r}} < v_J(\alpha) \\[4mm] 1 & \text{for} \quad \sqrt{\dfrac{\Delta V}{\alpha \rho_r}} \geq v_J(\alpha) \end{cases}
\tag{8.1}
$$
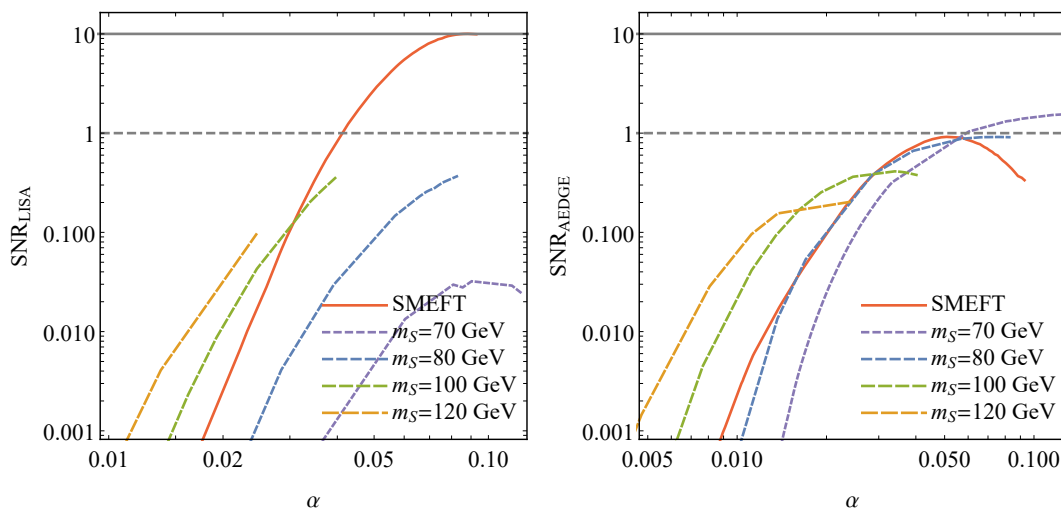
Figure 16. Signal to Noise Ratio for the GW backgrounds predicted by the singlet scalar and SMEFT models.
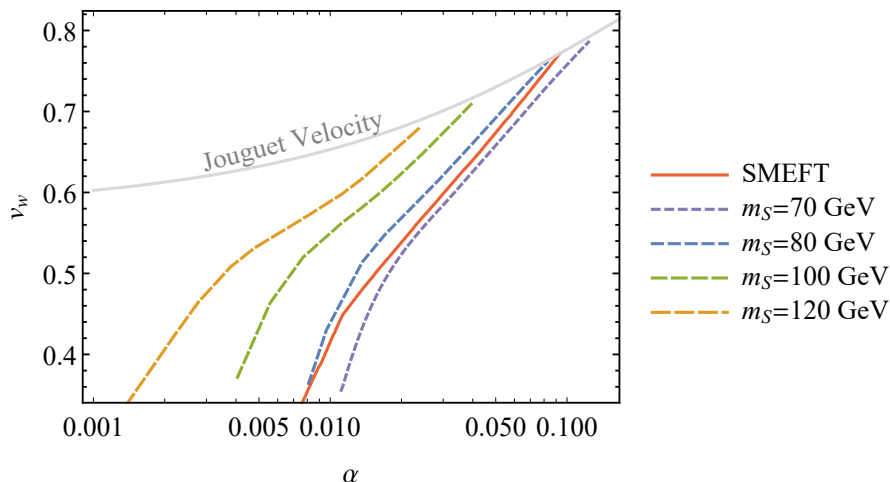

Figure 17. Bubble wall velocity solutions as a function of the phase transition strength α for all the models tested.

where $v_J(\alpha)$ is the Jouguet velocity from eq. (3.8). The lower case corresponds to transitions too strong for the fluid approximation to find a solution as discussed in section 4.2. We show in the left panel of figure 18 the comparison of this simple approximation with the results we find in all the SM extensions we studied. Although the level of agreement between the naive formula and our results might seem extraordinary at first, it is not difficult to understand. Reminding ourselves that the velocity is determined by finding the roots of the moments introduced in eqs. (4.16), (4.17) and that M_1 mostly fixes v_w as can be appreciated in figure (4), it is natural to ask what is the relation between M_1 and the approximation in eq. 8.1. The answer is that in thermal equilibrium the condition $M_1 = 0$ is simply equivalent to that formula. First we notice that if the temperature
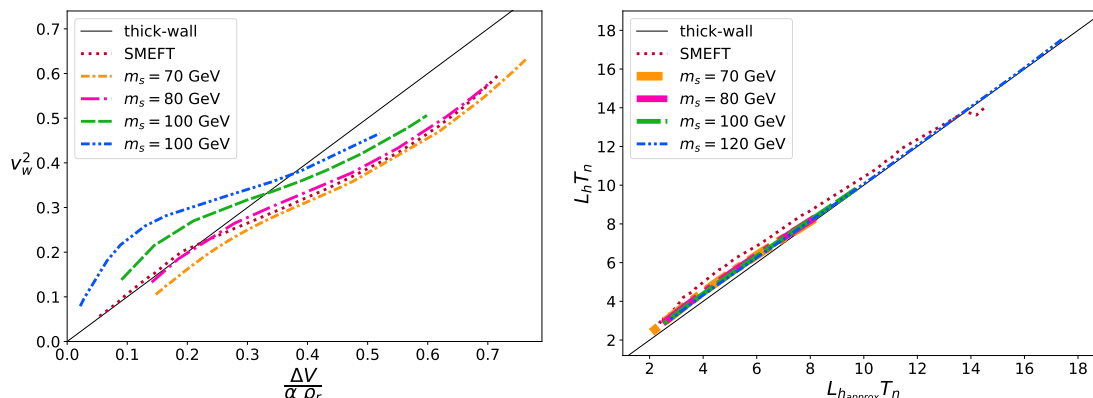
Figure 18. Left: comparison between the wall velocity calculation using the semiclassical method and the thermal equilibrium formula, eq. (8.1). Right: comparison between our results for the wall thickness in the Higgs direction with the estimated formula eq. (8.7). Both: the solid black line has slope one and is plotted for visual guidance.

remains constant we can write (4.16) as

$$M_1 = \int dz \frac{\partial T_\phi^{zz}}{\partial z} = \Delta T_\phi^{zz}, \qquad (8.2)$$

where T_ϕ^{zz} is the zz component of the energy momentum tensor of the scalar field, i.e. the momentum flux in the z direction. Now if one replaces the scalar field contribution, in the above formula, by that of a perfect fluid in thermal equilibrium one obtains instead

$$M_1 = \Delta\left(\omega\gamma^2 v^2 + p\right) = 0, \quad \rightarrow \quad -\Delta p = \gamma^2 v^2 \Delta\omega, \qquad (8.3)$$

where we used that in the steady state the wall has reached a constant velocity. Then using the relation $p = -V(\phi, T)$ together with the thermodynamic identity $\omega = T\frac{\partial p}{\partial T}$ and solving for the velocity we arrive at

$$v^2 = \frac{\Delta V(\phi, T)}{\Delta\left(V(\phi, T) - T\frac{\partial V(\phi, T)}{\partial T}\right)} \equiv \frac{\Delta V}{\alpha\rho_r}, \qquad (8.4)$$

where the definition of the strength, eq. (2.12) was used and we omitted the factor $1/4$ in the denominator. This gives us the first case in eq. 8.1. The fact that the above formula can provide a proxy for the wall velocity in some cases is tied to the assumption of small departure from equilibrium. If for a given strength, the above formula yields a velocity above the Jouguet value then the transition is too strong and there cannot be thermodynamic equilibrium. Let us also note that the above expression can be derived from recent results on the wall velocity in local equilibrium [98]. In particular, equating the two pressures in formula (17) of that reference and assuming constant velocity with thermal equilibrium one arrives at the same result.

Having obtained a usable formula for the wall velocity in thermal equilibrium, it is instructive to obtain an expression for the wall thickness using the second moment. Assuming

again constant temperature we can write eq. (4.17) as follows

$$M_2 = \int dz \ \partial_z T_\phi^{zz} \phi(z) = -V(\phi_0, T)\phi_0 - \int dz \frac{1}{2}(\partial_z \phi)^3 + \int dz V(\phi, T)\partial_z \phi, \qquad (8.5)$$

where in the last equality we simply integrated by parts. The second integral above simplifies to $\int \frac{1}{2}(\partial_z \phi)^3 = \phi_0^3/30L^2$ when using the tanh ansatz, then one can solve for the thickness

$$L^2 = \frac{\phi_0^3}{30 \left[\int V(\phi, T)d\phi - V(\phi_0, T)\phi_0\right]}. \qquad (8.6)$$

In the above derivation we have assumed the dependence on a single field ϕ, which in our case is identified with the Higgs but this expression can be generalized for multiple fields. We do not pursue the generalization here but instead notice that the expression in the denominator can be traded for the height of the potential barrier[5] thus $L^2 \propto \phi_0^2/V_h$ where V_h is the height. The proportionality constant is model dependent and we found that for the scalar singlet model and for SMEFT the best approximation is given by

$$L^2 = \frac{\phi_0^2}{4V_h}. \qquad (8.7)$$

To quantify the discrepancy of this approximation with our results for the scalar singlet we calculate the height of the potential barrier using the maximum value of the potential along the path of minimum energy at the critical temperature. In the numerator we used the expectation value of the field at the true vacuum. As we show in figure 18, eq. (8.7) provides an extremely good approximation for the width of the wall of the Higgs field.

In figure 19 we show the comparison of results from eq. (8.7) (with the numerator evaluated at the false vacuum, $s_0 \neq 0$) with our numerical results for the scalar singlet wall. Clearly the appropriate numerical constant in eq. (8.7) for this case depends on the mass of the scalar and so reproducing the details of the scalar singlet wall is more difficult than in the Higgs direction making full reproduction of the BAU from these simplifications difficult.

9 Summary and conclusions

In this paper we have investigated the FOPTs arising within the scalar singlet extension of the SM with parity symmetric potential and in the SMEFT with a dimension six operator. The bubble profile and its velocity were computed from first principles using the recently improved semiclassical fluid equations of Cline and Laurent [120]. The parameter space of the scalar singlet model has been thoroughly studied in ref. [121]. Here we did not undertake a full scan but instead focused on the qualitative features for some particularly motivated values of the scalar singlet mass. In the SMEFT the cutoff scale of the dimension six operator in the scalar potential is the only relevant parameter and we surveyed the whole range that facilitates a FOPT.

---

[5]To convince oneself, one can use as an example the simplest looking potential $V = \lambda/4\phi^2(\phi - \phi_0)^2$, See [118].
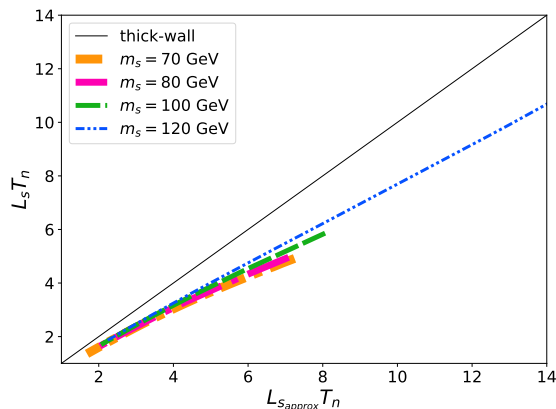
Figure 19. Comparison between our results for the wall thickness in the singlet direction with the estimated formula eq. (8.7). The solid black line has slope one and is plotted for visual guidance.

For both scenarios we have found the intuitive expectation that stronger transitions produce faster walls holds. However, the strength of the transition suitable for baryogenesis is severely limited with $\alpha \leq 0.1$. For stronger transitions the friction of the plasma does not cease the acceleration of the wall before it reaches the Jouguet velocity. Above that velocity the heated plasma shell around the bubble disappears as our hydrodynamic solution becomes a detonation. This lowers the plasma friction significantly and such walls always reach very relativistic velocity $v_w \geq 0.9$ for which we cannot compute the wall properties and assert the viability of baryogenesis. We find this behaviour in both models which suggests this could be a generic trademark of any SM-like model which does not modify the SM plasma contents drastically.

Our results also show that very strong transitions are not suitable for the semiclassical treatment as no solution for the moments can be found. In this case the assumptions of the fluid approximation are not satisfied as the wall becomes very thin and the WKB approximation is invalid. We also expect that very strong transitions correspond to large departures from thermodynamic equilibrium and a different formalism is needed in that case. In this paper we have focused only on the region of parameter space for which the wall properties can be computed. We have considered the presence of higher dimensional CP-violating operators and computed the BAU employing the upgraded fluid equations of [122]. While the scalar singlet model can easily yield the right amount of asymmetry, the EDM constraints on the CP-violating cutoff scale make SMEFT not capable of explaining the BAU.

Computation of the wall velocity is also crucial for the GW signals produced by the transition. We calculate the GW signals in both scenarios for transitions in which we can compute the properties of the wall. We find that only the strongest transitions of SMEFT fall within the sensitivity band of the LISA experiment while AEDGE operating at a slightly higher frequency will not be able to observe any of these signals. Both models, of course, support also stronger transitions which would be clearly visible in LISA and AEDGE, however, for these cases we find the plasma friction will not stop the wall acceleration

before breakdown of the fluid approximation and its justified to simply assume $v_w \approx 1$. We provide a simple and quite accurate approximation for the wall velocity requiring only the strength of the transition and potential which takes this effect into account. From our results we infer that GW signals produced by simple SM extensions visible in future experiments are likely to only be produced in strong transitions with $v_w \approx 1$. This does not mean that plasma can be neglected altogether in these results and bubble collision can always play an important role as this requires $\alpha \gg 1$ instead. However, observable signals produced by plasma related sources are likely to be produced mostly by detonations with highly relativistic wall velocities.

Acknowledgments

A Finite temperature effective potential

In this paper we adopt the customary procedure of calculating the effective potential in the Landau gauge where the contribution from the Goldstone bosons is independent from the massive gauge bosons and ghosts do not contribute.

Generically, the effective finite temperature potential is given by

$$V_{\text{eff}}(\phi, T) = V_0(\phi) + V_{\text{CW}}(\phi) + V_{\text{T}}(\phi, T). \tag{A.1}$$

where V_0 gives the tree-level contribution, V_{CW} represents the Coleman-Weinberg potential [176] and V_{T} the finite temperature contribution. In the equation above we have written a generic field dependence but it should be understood that ϕ could denote the background field values h and s in the scalar singlet extension or simply the Higgs background vev in case of the SMEFT.

In this paper we consider the effective potential calculated at one-loop order and we choose to follow the on-shell prescription [143, 177] in which the one-loop contributions do not disturb the minimization conditions at tree-level. In this case, the Coleman-Weinberg contribution can be written as

$$V_{\text{CW}}(\phi) = \sum_i (-1)^{F_i} \frac{d_i}{64\pi^2} \left[m_i^4(\phi) \left(\log \frac{m_i^2(\phi)}{m_{0i}^2} - \frac{3}{2} \right) + 2m_i^2(\phi)m_{0i}^2 \right], \tag{A.2}$$

where the index i runs over all particles contributing to the potential with $F_i = 0$ (1) for bosons (fermions), d_i is the number of degrees of freedom of the particle species while $m_i(\phi)$ is the field dependent mass of particle i and m_{0i} its value at the EW vacuum. As mentioned above, this form of the Coleman-Weinberg potential ensures that the zero

temperature vacuum conditions are completely determined by the tree-level contribution. In other words

$$\frac{dV_{\mathrm{CW}}(\phi)}{d\phi}\bigg|_{\phi_0} = \frac{d^2V_{\mathrm{CW}}(\phi)}{d\phi^2}\bigg|_{\phi_0} = 0, \tag{A.3}$$

where ϕ_0 corresponds to the field values at the zero temperature EW vacuum, i.e., $\phi_0 = (v, 0)$ for scalar singlet and $\phi_0 = v$ in the SMEFT.

The contribution to the Coleman-Weinberg potential from the Goldstone bosons requires special care since for small field values the squared mass parameter becomes negative and furthermore it vanishes at the EWSB minimum leading to infrared divergences of the effective potential. It has been shown in [178, 179] that proper resummation of the Goldstone boson contributions must be performed to avoid such divergences. We do not include the contributions from the Goldstone bosons as it has been shown [179] that the numerical impact of the resummation procedure as a function of the renormalization scale is very small.

The finite temperature piece is given by

$$V_T(\phi, T) = \frac{T^4}{2\pi^2}\sum_i d_i J_{\mp}\left(\frac{m_i(\phi)}{T}\right), \tag{A.4}$$

where the $J_{\mp}$ functions are defined as

$$J_{\mp}(x) = \pm \int_0^\infty dy\, y^2 \log\left(1 \mp e^{-\sqrt{y^2+x^2}}\right), \tag{A.5}$$

and the upper (lower) sign is for bosons (fermions).

The well known breakdown of the perturbative expansion at high temperature [180] due to the presence of infrared bosonic modes can be ameliorated by performing dimensional reduction techniques [68, 181, 182]. Such a dedicated study is left for future work.

B Field dependent and thermal masses

In this section we present the relevant formulas for the field dependent masses which are inputs for the one-loop and thermal contributions to the effective potential. In the models studied in this paper the thermal masses for the SM particles are given by

$$m_W^2 = \frac{g^2}{4}h^2, \quad m_Z^2 = \frac{g^2 + g'^2}{4}h^2, \quad m_t^2 = \frac{y_t^2}{2}h^2. \tag{B.1}$$

The field dependent masses for the scalar particles are modified with respect to the SM and are presented in the following two sub-appendices.

B.1 Scalar singlet extension

At any field value the physical masses correspond to the eigenvalues of the Hessian matrix of the scalar potential, namely

$$m_{ij}^2(h, s) = \begin{pmatrix} \frac{m_h^2}{2}\left(3\frac{h^2}{v^2} - 1\right) + s^2\frac{\lambda_{hs}}{2} & hs\lambda_{hs} \\ hs\lambda_{hs} & m_s^2 + \frac{h^2 - v^2}{2}\lambda_{hs} + 3\lambda_s s^2 \end{pmatrix}. \tag{B.2}$$

We add the effect of thermal masses that correct the behavior at high temperatures. In our model they are written as [183, 184]

$$\Pi_h = \left(\frac{3g^2}{16} + \frac{g'^2}{16} + \frac{\lambda}{2} + \frac{y_t^2}{4} + \frac{\lambda_{hs}}{24} \right) T^2, \tag{B.3}$$

$$\Pi_s = \left(\frac{\lambda_{hs}}{6} + \frac{\lambda_s}{4} \right) T^2, \tag{B.4}$$

$$\Pi_{\text{Gauge}} = T^2 \text{diag}\left(\frac{11}{6} g^2, \frac{11}{6} g'^2 \right). \tag{B.5}$$

A truncated full dressing implementation [185] amounts to the replacement

$$m_{ii}^2(h, s) \to m_{ij}^2(h, s, T) \equiv m_{ii}^2(h, s) + \Pi_i \tag{B.6}$$

in the one-loop potential at finite temperature. This procedure is also called daisy resummation.

B.2 SMEFT

In this model the addition of the dimension six operator gives rise to a Higgs mass

$$m_h^2 = -m^2 + 3\lambda h^2 + \frac{15}{4} \frac{h^4}{\Lambda^2}, \tag{B.7}$$

while the thermal masses are

$$\Pi_h(T) = \frac{T^2}{4v^2} \left(m_h^2 + 2m_W^2 + m_Z^2 + 2m_t^2 \right) - \frac{3}{4} T^2 \frac{v^2}{\Lambda^2}, \\ \Pi_W(T) = \frac{22}{3} \frac{m_W^2}{v^2} T^2. \tag{B.8}$$

References

[1] M.J. Baker, J. Kopp and A.J. Long, *Filtered dark matter at a first order phase transition*, *Phys. Rev. Lett.* **125** (2020) 151102 [arXiv:1912.02830] [INSPIRE].

[2] I. Baldes, Y. Gouttenoire and F. Sala, *String fragmentation in supercooled confinement and implications for dark matter*, *JHEP* **04** (2021) 278 [arXiv:2007.08440] [INSPIRE].

[3] A. Azatov, M. Vanvlasselaer and W. Yin, *Dark matter production from relativistic bubble walls*, *JHEP* **03** (2021) 288 [arXiv:2101.05721] [INSPIRE].

[4] M. Ahmadvand, *Filtered asymmetric dark matter during the Peccei-Quinn phase transition*, *JHEP* **10** (2021) 109 [arXiv:2108.00958] [INSPIRE].

[5] A.G. Cohen, D.B. Kaplan and A.E. Nelson, *Progress in electroweak baryogenesis*, *Ann. Rev. Nucl. Part. Sci.* **43** (1993) 27 [hep-ph/9302210] [INSPIRE].

[6] V.A. Kuzmin, V.A. Rubakov and M.E. Shaposhnikov, *On the anomalous electroweak baryon number nonconservation in the early universe*, *Phys. Lett. B* **155** (1985) 36 [INSPIRE].

[7] V.A. Rubakov and M.E. Shaposhnikov, *Electroweak baryon number nonconservation in the early universe and in high-energy collisions*, *Usp. Fiz. Nauk* **166** (1996) 493 [hep-ph/9603208] [INSPIRE].

[8] D.E. Morrissey and M.J. Ramsey-Musolf, *Electroweak baryogenesis*, *New J. Phys.* **14** (2012) 125003 [arXiv:1206.2942] [INSPIRE].

[9] P. Di Bari, D. Marfatia and Y.-L. Zhou, *Gravitational waves from neutrino mass and dark matter genesis*, *Phys. Rev. D* **102** (2020) 095017 [arXiv:2001.07637] [INSPIRE].

[10] E. Witten, *Cosmic separation of phases*, *Phys. Rev. D* **30** (1984) 272 [INSPIRE].

[11] LIGO SCIENTIFIC, VIRGO collaboration, *GW170817: observation of gravitational waves from a binary neutron star inspiral*, *Phys. Rev. Lett.* **119** (2017) 161101 [arXiv:1710.05832] [INSPIRE].

[12] LIGO SCIENTIFIC, VIRGO collaboration, *GWTC-2: compact binary coalescences observed by LIGO and Virgo during the first half of the third observing run*, *Phys. Rev. X* **11** (2021) 021053 [arXiv:2010.14527] [INSPIRE].

[13] NANOGRAV collaboration, *The NANOGrav 12.5 yr data set: search for an isotropic stochastic gravitational-wave background*, *Astrophys. J. Lett.* **905** (2020) L34 [arXiv:2009.04496] [INSPIRE].

[14] B. Goncharov et al., *On the evidence for a common-spectrum process in the search for the nanohertz gravitational-wave background with the Parkes pulsar Timing Array*, *Astrophys. J. Lett.* **917** (2021) L19 [arXiv:2107.12112] [INSPIRE].

[15] J. Ellis and M. Lewicki, *Cosmic string interpretation of NANOGrav pulsar timing data*, *Phys. Rev. Lett.* **126** (2021) 041304 [arXiv:2009.06555] [INSPIRE].

[16] S. Blasi, V. Brdar and K. Schmitz, *Has NANOGrav found first evidence for cosmic strings?*, *Phys. Rev. Lett.* **126** (2021) 041305 [arXiv:2009.06607] [INSPIRE].

[17] V. Vaskonen and H. Veermäe, *Did NANOGrav see a signal from primordial black hole formation?*, *Phys. Rev. Lett.* **126** (2021) 051303 [arXiv:2009.07832] [INSPIRE].

[18] V. De Luca, G. Franciolini and A. Riotto, *NANOGrav data hints at primordial black holes as dark matter*, *Phys. Rev. Lett.* **126** (2021) 041303 [arXiv:2009.08268] [INSPIRE].

[19] Y. Nakai, M. Suzuki, F. Takahashi and M. Yamada, *Gravitational waves and dark radiation from dark phase transition: connecting NANOGrav pulsar timing data and Hubble tension*, *Phys. Lett. B* **816** (2021) 136238 [arXiv:2009.09754] [INSPIRE].

[20] W. Ratzinger and P. Schwaller, *Whispers from the dark side: confronting light new physics with NANOGrav data*, *SciPost Phys.* **10** (2021) 047 [arXiv:2009.11875] [INSPIRE].

[21] K. Kohri and T. Terada, *Solar-mass primordial black holes explain NANOGrav hint of gravitational waves*, *Phys. Lett. B* **813** (2021) 136040 [arXiv:2009.11853] [INSPIRE].

[22] S. Vagnozzi, *Implications of the NANOGrav results for inflation*, *Mon. Not. Roy. Astron. Soc.* **502** (2021) L11 [arXiv:2009.13432] [INSPIRE].

[23] A. Neronov, A. Roper Pol, C. Caprini and D. Semikoz, *NANOGrav signal from magnetohydrodynamic turbulence at the QCD phase transition in the early Universe*, *Phys. Rev. D* **103** (2021) 041302 [arXiv:2009.14174] [INSPIRE].

[24] H. Middleton, A. Sesana, S. Chen, A. Vecchio, W. Del Pozzo and P.A. Rosado, *Massive black hole binary systems and the NANOGrav 12.5 yr results*, *Mon. Not. Roy. Astron. Soc.* **502** (2021) L99 [arXiv:2011.01246] [INSPIRE].

[25] C. Grojean and G. Servant, *Gravitational waves from phase transitions at the electroweak scale and beyond*, *Phys. Rev. D* **75** (2007) 043507 [`hep-ph/0607107`] [inSPIRE].

[26] J.R. Espinosa, T. Konstandin, J.M. No and M. Quirós, *Some cosmological implications of hidden sectors*, *Phys. Rev. D* **78** (2008) 123528 [`arXiv:0809.3215`] [inSPIRE].

[27] G.C. Dorsch, S.J. Huber and J.M. No, *Cosmological signatures of a UV-conformal standard model*, *Phys. Rev. Lett.* **113** (2014) 121801 [`arXiv:1403.5583`] [inSPIRE].

[28] J. Jaeckel, V.V. Khoze and M. Spannowsky, *Hearing the signal of dark sectors with gravitational wave detectors*, *Phys. Rev. D* **94** (2016) 103519 [`arXiv:1602.03901`] [inSPIRE].

[29] R. Jinno and M. Takimoto, *Probing a classically conformal B-L model with gravitational waves*, *Phys. Rev. D* **95** (2017) 015020 [`arXiv:1604.05035`] [inSPIRE].

[30] M. Chala, G. Nardini and I. Sobolev, *Unified explanation for dark matter and electroweak baryogenesis with direct detection and gravitational wave signatures*, *Phys. Rev. D* **94** (2016) 055006 [`arXiv:1605.08663`] [inSPIRE].

[31] M. Chala, M. Ramos and M. Spannowsky, *Gravitational wave and collider probes of a triplet Higgs sector with a low cutoff*, *Eur. Phys. J. C* **79** (2019) 156 [`arXiv:1812.01901`] [inSPIRE].

[32] M. Artymowski, M. Lewicki and J.D. Wells, *Gravitational wave and collider implications of electroweak baryogenesis aided by non-standard cosmology*, *JHEP* **03** (2017) 066 [`arXiv:1609.07143`] [inSPIRE].

[33] K. Hashino, M. Kakizaki, S. Kanemura, P. Ko and T. Matsui, *Gravitational waves and Higgs boson couplings for exploring first order phase transition in the model with a singlet scalar field*, *Phys. Lett. B* **766** (2017) 49 [`arXiv:1609.00297`] [inSPIRE].

[34] V. Vaskonen, *Electroweak baryogenesis and gravitational waves from a real scalar singlet*, *Phys. Rev. D* **95** (2017) 123515 [`arXiv:1611.02073`] [inSPIRE].

[35] G.C. Dorsch, S.J. Huber, T. Konstandin and J.M. No, *A second Higgs doublet in the early universe: baryogenesis and gravitational waves*, *JCAP* **05** (2017) 052 [`arXiv:1611.05874`] [inSPIRE].

[36] A. Beniwal, M. Lewicki, J.D. Wells, M. White and A.G. Williams, *Gravitational wave, collider and dark matter signals from a scalar singlet electroweak baryogenesis*, *JHEP* **08** (2017) 108 [`arXiv:1702.06124`] [inSPIRE].

[37] I. Baldes, *Gravitational waves from the asymmetric-dark-matter generating phase transition*, *JCAP* **05** (2017) 028 [`arXiv:1702.02117`] [inSPIRE].

[38] L. Marzola, A. Racioppi and V. Vaskonen, *Phase transition and gravitational wave phenomenology of scalar conformal extensions of the Standard Model*, *Eur. Phys. J. C* **77** (2017) 484 [`arXiv:1704.01034`] [inSPIRE].

[39] Z. Kang, P. Ko and T. Matsui, *Strong first order EWPT & strong gravitational waves in Z_3-symmetric singlet scalar extension*, *JHEP* **02** (2018) 115 [`arXiv:1706.09721`] [inSPIRE].

[40] S. Iso, P.D. Serpico and K. Shimada, *QCD-Electroweak First-Order Phase Transition in a Supercooled Universe*, *Phys. Rev. Lett.* **119** (2017) 141301 [`arXiv:1704.04955`] [inSPIRE].

[41] M. Chala, C. Krause and G. Nardini, *Signals of the electroweak phase transition at colliders and gravitational wave observatories*, *JHEP* **07** (2018) 062 [`arXiv:1802.02168`] [inSPIRE].

[42] S. Bruggisser, B. Von Harling, O. Matsedonskyi and G. Servant, *Electroweak phase transition and baryogenesis in composite Higgs models*, *JHEP* **12** (2018) 099 [`arXiv:1804.07314`] [inSPIRE].

[43] E. Megías, G. Nardini and M. Quirós, *Cosmological phase transitions in warped space: gravitational waves and collider signatures*, *JHEP* **09** (2018) 095 [arXiv:1806.04877] [INSPIRE].

[44] D. Croon, V. Sanz and G. White, *Model discrimination in gravitational wave spectra from dark phase transitions*, *JHEP* **08** (2018) 203 [arXiv:1806.02332] [INSPIRE].

[45] A. Alves, T. Ghosh, H.-K. Guo, K. Sinha and D. Vagie, *Collider and gravitational wave complementarity in exploring the singlet extension of the standard model*, *JHEP* **04** (2019) 052 [arXiv:1812.09333] [INSPIRE].

[46] P. Baratella, A. Pomarol and F. Rompineve, *The supercooled universe*, *JHEP* **03** (2019) 100 [arXiv:1812.06996] [INSPIRE].

[47] A. Angelescu and P. Huang, *Multistep strongly first order phase transitions from new fermions at the TeV scale*, *Phys. Rev. D* **99** (2019) 055023 [arXiv:1812.08293] [INSPIRE].

[48] D. Croon, T.E. Gonzalo and G. White, *Gravitational waves from a Pati-Salam phase transition*, *JHEP* **02** (2019) 083 [arXiv:1812.02747] [INSPIRE].

[49] V. Brdar, A.J. Helmboldt and J. Kubo, *Gravitational Waves from first-order phase transitions: LIGO as a window to unexplored seesaw scales*, *JCAP* **02** (2019) 021 [arXiv:1810.12306] [INSPIRE].

[50] A. Beniwal, M. Lewicki, M. White and A.G. Williams, *Gravitational waves and electroweak baryogenesis in a global study of the extended scalar singlet model*, *JHEP* **02** (2019) 183 [arXiv:1810.02380] [INSPIRE].

[51] M. Breitbach, J. Kopp, E. Madge, T. Opferkuch and P. Schwaller, *Dark, Cold, and Noisy: Constraining Secluded Hidden Sectors with Gravitational Waves*, *JCAP* **07** (2019) 007 [arXiv:1811.11175] [INSPIRE].

[52] C. Marzo, L. Marzola and V. Vaskonen, *Phase transition and vacuum stability in the classically conformal B-L model*, *Eur. Phys. J. C* **79** (2019) 601 [arXiv:1811.11169] [INSPIRE].

[53] I. Baldes and C. Garcia-Cely, *Strong gravitational radiation from a simple dark matter model*, *JHEP* **05** (2019) 190 [arXiv:1809.01198] [INSPIRE].

[54] T. Prokopec, J. Rezacek and B. Świeżewska, *Gravitational waves from conformal symmetry breaking*, *JCAP* **02** (2019) 009 [arXiv:1809.11129] [INSPIRE].

[55] M. Fairbairn, E. Hardy and A. Wickens, *Hearing without seeing: gravitational waves from hot and cold hidden sectors*, *JHEP* **07** (2019) 044 [arXiv:1901.11038] [INSPIRE].

[56] A.J. Helmboldt, J. Kubo and S. van der Woude, *Observational prospects for gravitational waves from hidden or dark chiral phase transitions*, *Phys. Rev. D* **100** (2019) 055025 [arXiv:1904.07891] [INSPIRE].

[57] P.S.B. Dev, F. Ferrer, Y. Zhang and Y. Zhang, *Gravitational waves from first-order phase transition in a simple axion-like particle model*, *JCAP* **11** (2019) 006 [arXiv:1905.00891] [INSPIRE].

[58] S.A.R. Ellis, S. Ipek and G. White, *Electroweak baryogenesis from temperature-varying couplings*, *JHEP* **08** (2019) 002 [arXiv:1905.11994] [INSPIRE].

[59] R. Jinno, T. Konstandin and M. Takimoto, *Relativistic bubble collisions — A closer look*, *JCAP* **09** (2019) 035 [arXiv:1906.02588] [INSPIRE].

[60] J. Ellis, M. Fairbairn, M. Lewicki, V. Vaskonen and A. Wickens, *Intergalactic magnetic fields from first-order phase transitions*, *JCAP* **09** (2019) 019 [arXiv:1907.04315] [INSPIRE].

[61] A. Azatov, D. Barducci and F. Sgarlata, *Gravitational traces of broken gauge symmetries*, *JCAP* **07** (2020) 027 [arXiv:1910.01124] [INSPIRE].

[62] B. Von Harling, A. Pomarol, O. Pujolàs and F. Rompineve, *Peccei-Quinn Phase Transition at LIGO*, *JHEP* **04** (2020) 195 [arXiv:1912.07587] [INSPIRE].

[63] L. Delle Rose, G. Panico, M. Redi and A. Tesi, *Gravitational waves from supercool axions*, *JHEP* **04** (2020) 025 [arXiv:1912.06139] [INSPIRE].

[64] M. Barroso Mancha, T. Prokopec and B. Swiezewska, *Field-theoretic derivation of bubble-wall force*, *JHEP* **01** (2021) 070 [arXiv:2005.10875] [INSPIRE].

[65] A. Azatov and M. Vanvlasselaer, *Bubble wall velocity: heavy physics effects*, *JCAP* **01** (2021) 058 [arXiv:2010.02590] [INSPIRE].

[66] F. Giese, T. Konstandin, K. Schmitz and J. Van De Vis, *Model-independent energy budget for LISA*, *JCAP* **01** (2021) 072 [arXiv:2010.09744] [INSPIRE].

[67] S. Höche, J. Kozaczuk, A.J. Long, J. Turner and Y. Wang, *Towards an all-orders calculation of the electroweak bubble wall velocity*, *JCAP* **03** (2021) 009 [arXiv:2007.10343] [INSPIRE].

[68] D. Croon, O. Gould, P. Schicho, T.V.I. Tenkanen and G. White, *Theoretical uncertainties for cosmological first-order phase transitions*, *JHEP* **04** (2021) 055 [arXiv:2009.10080] [INSPIRE].

[69] F.R. Ares, M. Hindmarsh, C. Hoyos and N. Jokela, *Gravitational waves from a holographic phase transition*, *JHEP* **21** (2020) 100 [arXiv:2011.12878] [INSPIRE].

[70] R.-G. Cai and S.-J. Wang, *Effective picture of bubble expansion*, *JCAP* **03** (2021) 096 [arXiv:2011.11451] [INSPIRE].

[71] F. Bigazzi, A. Caddeo, A.L. Cotrone and A. Paredes, *Dark holograms and gravitational waves*, *JHEP* **04** (2021) 094 [arXiv:2011.08757] [INSPIRE].

[72] X. Wang, F.P. Huang and X. Zhang, *Bubble wall velocity beyond leading-log approximation in electroweak phase transition*, arXiv:2011.12903 [INSPIRE].

[73] I. Baldes, Y. Gouttenoire, F. Sala and G. Servant, *Supercool composite dark matter beyond 100 TeV*, arXiv:2110.13926 [INSPIRE].

[74] C. Caprini et al., *Science with the space-based interferometer eLISA. II: Gravitational waves from cosmological phase transitions*, *JCAP* **04** (2016) 001 [arXiv:1512.06239] [INSPIRE].

[75] C. Caprini et al., *Detecting gravitational waves from cosmological phase transitions with LISA: an update*, *JCAP* **03** (2020) 024 [arXiv:1910.13125] [INSPIRE].

[76] S.R. Coleman, *The fate of the false vacuum. 1. Semiclassical theory*, *Phys. Rev. D* **15** (1977) 2929 [*Erratum ibid.* **16** (1977) 1248] [INSPIRE].

[77] C.G. Callan, Jr. and S.R. Coleman, *The fate of the false vacuum. 2. First quantum corrections*, *Phys. Rev. D* **16** (1977) 1762 [INSPIRE].

[78] A.D. Linde, *Decay of the false vacuum at finite temperature*, *Nucl. Phys. B* **216** (1983) 421 [*Erratum ibid.* **223** (1983) 544] [INSPIRE].

[79] A. Kosowsky and M.S. Turner, *Gravitational radiation from colliding vacuum bubbles: envelope approximation to many bubble collisions*, *Phys. Rev. D* **47** (1993) 4372 [astro-ph/9211004] [INSPIRE].

[80] D. Cutting, M. Hindmarsh and D.J. Weir, *Gravitational waves from vacuum first-order phase transitions: from the envelope to the lattice*, *Phys. Rev. D* **97** (2018) 123513 [arXiv:1802.05712] [INSPIRE].

[81] J. Ellis, M. Lewicki, J.M. No and V. Vaskonen, *Gravitational wave energy budget in strongly supercooled phase transitions*, *JCAP* **06** (2019) 024 [arXiv:1903.09642] [INSPIRE].

[82] M. Lewicki and V. Vaskonen, *On bubble collisions in strongly supercooled phase transitions*, *Phys. Dark Univ.* **30** (2020) 100672 [arXiv:1912.00997] [INSPIRE].

[83] D. Cutting, E.G. Escartin, M. Hindmarsh and D.J. Weir, *Gravitational waves from vacuum first order phase transitions II: from thin to thick walls*, *Phys. Rev. D* **103** (2021) 023531 [arXiv:2005.13537] [INSPIRE].

[84] M. Lewicki and V. Vaskonen, *Gravitational wave spectra from strongly supercooled phase transitions*, *Eur. Phys. J. C* **80** (2020) 1003 [arXiv:2007.04967] [INSPIRE].

[85] J. Ellis, M. Lewicki and V. Vaskonen, *Updated predictions for gravitational waves produced in a strongly supercooled phase transition*, *JCAP* **11** (2020) 020 [arXiv:2007.15586] [INSPIRE].

[86] M. Kamionkowski, A. Kosowsky and M.S. Turner, *Gravitational radiation from first order phase transitions*, *Phys. Rev. D* **49** (1994) 2837 [astro-ph/9310044] [INSPIRE].

[87] M. Hindmarsh, S.J. Huber, K. Rummukainen and D.J. Weir, *Numerical simulations of acoustically generated gravitational waves at a first order phase transition*, *Phys. Rev. D* **92** (2015) 123009 [arXiv:1504.03291] [INSPIRE].

[88] M. Hindmarsh, *Sound shell model for acoustic gravitational wave production at a first-order phase transition in the early Universe*, *Phys. Rev. Lett.* **120** (2018) 071301 [arXiv:1608.04735] [INSPIRE].

[89] M. Hindmarsh, S.J. Huber, K. Rummukainen and D.J. Weir, *Shape of the acoustic gravitational wave power spectrum from a first order phase transition*, *Phys. Rev. D* **96** (2017) 103520 [*Erratum ibid.* **101** (2020) 089902] [arXiv:1704.05871] [INSPIRE].

[90] J. Ellis, M. Lewicki and J.M. No, *On the maximal strength of a first-order electroweak phase transition and its gravitational wave signal*, *JCAP* **04** (2019) 003 [arXiv:1809.08242] [INSPIRE].

[91] M. Hindmarsh and M. Hijazi, *Gravitational waves from first order cosmological phase transitions in the Sound Shell Model*, *JCAP* **12** (2019) 062 [arXiv:1909.10040] [INSPIRE].

[92] J. Ellis, M. Lewicki and J.M. No, *Gravitational waves from first-order cosmological phase transitions: lifetime of the sound wave source*, *JCAP* **07** (2020) 050 [arXiv:2003.07360] [INSPIRE].

[93] M. Dine, P. Huet, R.L. Singleton Jr. and L. Susskind, *Creating the baryon asymmetry at the electroweak phase transition*, *Phys. Lett. B* **257** (1991) 351 [INSPIRE].

[94] M. Dine, R.G. Leigh, P.Y. Huet, A.D. Linde and D.A. Linde, *Towards the theory of the electroweak phase transition*, *Phys. Rev. D* **46** (1992) 550 [hep-ph/9203203] [INSPIRE].

[95] B.-H. Liu, L.D. McLerran and N. Turok, *Bubble nucleation and growth at a baryon number producing electroweak phase transition*, *Phys. Rev. D* **46** (1992) 2668 [INSPIRE].

[96] T. Konstandin and J.M. No, *Hydrodynamic obstruction to bubble expansion*, *JCAP* **02** (2011) 008 [arXiv:1011.3735] [INSPIRE].

[97] S. Balaji, M. Spannowsky and C. Tamarit, *Cosmological bubble friction in local equilibrium*, *JCAP* **03** (2021) 051 [arXiv:2010.08013] [INSPIRE].

[98] W.-Y. Ai, B. Garbrecht and C. Tamarit, *Bubble wall velocities in local equilibrium*, arXiv:2109.13710 [INSPIRE].

[99] P.B. Arnold, *One loop fluctuation-dissipation formula for bubble wall velocity*, *Phys. Rev. D* **48** (1993) 1539 [hep-ph/9302258] [INSPIRE].

[100] D. Bödeker and G.D. Moore, *Can electroweak bubble walls run away?*, *JCAP* **05** (2009) 009 [arXiv:0903.4099] [INSPIRE].

[101] D. Bödeker and G.D. Moore, *Electroweak bubble wall speed limit*, *JCAP* **05** (2017) 025 [arXiv:1703.08215] [INSPIRE].

[102] Y. Bea, J. Casalderrey-Solana, T. Giannakopoulos, D. Mateos, M. Sanchez-Garitaonandia and M. Zilhão, *Bubble wall velocity from holography*, *Phys. Rev. D* **104** (2021) L121903 [arXiv:2104.05708] [INSPIRE].

[103] F. Bigazzi, A. Caddeo, T. Canneti and A.L. Cotrone, *Bubble wall velocity at strong coupling*, *JHEP* **08** (2021) 090 [arXiv:2104.12817] [INSPIRE].

[104] N. Turok, *Electroweak bubbles: nucleation and growth*, *Phys. Rev. Lett.* **68** (1992) 1803 [INSPIRE].

[105] G.D. Moore and T. Prokopec, *Bubble wall velocity in a first order electroweak phase transition*, *Phys. Rev. Lett.* **75** (1995) 777 [hep-ph/9503296] [INSPIRE].

[106] P.J. Steinhardt, *Relativistic detonation waves and bubble growth in false vacuum decay*, *Phys. Rev. D* **25** (1982) 2074 [INSPIRE].

[107] J.R. Espinosa, T. Konstandin, J.M. No and G. Servant, *Energy budget of cosmological first-order phase transitions*, *JCAP* **06** (2010) 028 [arXiv:1004.4187] [INSPIRE].

[108] K. Enqvist, J. Ignatius, K. Kajantie and K. Rummukainen, *Nucleation and bubble growth in a first order cosmological electroweak phase transition*, *Phys. Rev. D* **45** (1992) 3415 [INSPIRE].

[109] J. Ignatius, K. Kajantie, H. Kurki-Suonio and M. Laine, *The growth of bubbles in cosmological phase transitions*, *Phys. Rev. D* **49** (1994) 3854 [astro-ph/9309059] [INSPIRE].

[110] G.D. Moore and T. Prokopec, *How fast can the wall move? A study of the electroweak phase transition dynamics*, *Phys. Rev. D* **52** (1995) 7182 [hep-ph/9506475] [INSPIRE].

[111] T. Konstandin, G. Nardini and I. Rues, *From Boltzmann equations to steady wall velocities*, *JCAP* **09** (2014) 028 [arXiv:1407.3132] [INSPIRE].

[112] J. Kozaczuk, *Bubble expansion and the viability of singlet-driven electroweak baryogenesis*, *JHEP* **10** (2015) 135 [arXiv:1506.04741] [INSPIRE].

[113] G.C. Dorsch, S.J. Huber and T. Konstandin, *Bubble wall velocities in the standard model and beyond*, *JCAP* **12** (2018) 034 [arXiv:1809.04907] [INSPIRE].

[114] A. Megevand and A.D. Sanchez, *Detonations and deflagrations in cosmological phase transitions*, *Nucl. Phys. B* **820** (2009) 47 [arXiv:0904.1753] [INSPIRE].

[115] A. Megevand and A.D. Sanchez, *Velocity of electroweak bubble walls*, *Nucl. Phys. B* **825** (2010) 151 [arXiv:0908.3663] [INSPIRE].

[116] M. Sopena and S.J. Huber, *Hydrodynamics of the electroweak phase transition in an extension of the standard model with dimension-6 interactions*, *J. Phys. Conf. Ser.* **259** (2010) 012048 [INSPIRE].

[117] A. Megevand and A.D. Sanchez, *Analytic approach to the motion of cosmological phase transition fronts*, *Nucl. Phys. B* **865** (2012) 217 [arXiv:1206.2339] [INSPIRE].

[118] S.J. Huber and M. Sopena, *An efficient approach to electroweak bubble velocities*, arXiv:1302.1044 [ɪɴSPIRE].

[119] A. Mégevand, *Friction forces on phase transition fronts*, *JCAP* **07** (2013) 045 [arXiv:1303.4233] [ɪɴSPIRE].

[120] B. Laurent and J.M. Cline, *Fluid equations for fast-moving electroweak bubble walls*, *Phys. Rev. D* **102** (2020) 063516 [arXiv:2007.10935] [ɪɴSPIRE].

[121] J.M. Cline, A. Friedlander, D.-M. He, K. Kainulainen, B. Laurent and D. Tucker-Smith, *Baryogenesis and gravity waves from a UV-completed electroweak phase transition*, *Phys. Rev. D* **103** (2021) 123529 [arXiv:2102.12490] [ɪɴSPIRE].

[122] J.M. Cline and K. Kainulainen, *Electroweak baryogenesis at high bubble wall velocities*, *Phys. Rev. D* **101** (2020) 063525 [arXiv:2001.00568] [ɪɴSPIRE].

[123] A.D. Linde, *Fate of the false vacuum at finite temperature: theory and applications*, *Phys. Lett. B* **100** (1981) 37 [ɪɴSPIRE].

[124] K. Saikawa and S. Shirai, *Primordial gravitational waves, precisely: The role of thermodynamics in the Standard Model*, *JCAP* **05** (2018) 035 [arXiv:1803.01038] [ɪɴSPIRE].

[125] G.R. Farrar and M.E. Shaposhnikov, *Baryon asymmetry of the universe in the standard electroweak theory*, *Phys. Rev. D* **50** (1994) 774 [hep-ph/9305275] [ɪɴSPIRE].

[126] M. Quirós, *Finite temperature field theory and phase transitions*, in *ICTP Summer School in High-Energy Physics and Cosmology*, pp. 187–259, 1, 1999 [hep-ph/9901312] [ɪɴSPIRE].

[127] K. Funakubo and E. Senaha, *Electroweak phase transition, critical bubbles and sphaleron decoupling condition in the MSSM*, *Phys. Rev. D* **79** (2009) 115024 [arXiv:0905.2022] [ɪɴSPIRE].

[128] K. Fuyuto and E. Senaha, *Improved sphaleron decoupling condition and the Higgs coupling constants in the real singlet-extended standard model*, *Phys. Rev. D* **90** (2014) 015015 [arXiv:1406.0433] [ɪɴSPIRE].

[129] J.M. No, *Large gravitational wave background signals in electroweak baryogenesis scenarios*, *Phys. Rev. D* **84** (2011) 124025 [arXiv:1103.2159] [ɪɴSPIRE].

[130] A. Friedlander, I. Banta, J.M. Cline and D. Tucker-Smith, *Wall speed and shape in singlet-assisted strong electroweak phase transitions*, *Phys. Rev. D* **103** (2021) 055020 [arXiv:2009.14295] [ɪɴSPIRE].

[131] L. Fromme and S.J. Huber, *Top transport in electroweak baryogenesis*, *JHEP* **03** (2007) 049 [hep-ph/0604159] [ɪɴSPIRE].

[132] G.C. Dorsch, S.J. Huber and T. Konstandin, *On the wall velocity dependence of electroweak baryogenesis*, *JCAP* **08** (2021) 020 [arXiv:2106.06547] [ɪɴSPIRE].

[133] G.C. Dorsch, S.J. Huber and T. Konstandin, *A sonic boom in bubble wall friction*, arXiv:2112.12548 [ɪɴSPIRE].

[134] J.M. Cline, M. Joyce and K. Kainulainen, *Supersymmetric electroweak baryogenesis*, *JHEP* **07** (2000) 018 [hep-ph/0006119] [ɪɴSPIRE].

[135] M.B. Hindmarsh, M. Lüben, J. Lumma and M. Pauly, *Phase transitions in the early universe*, *SciPost Phys. Lect. Notes* **24** (2021) 1 [arXiv:2008.09136] [ɪɴSPIRE].

[136] C.L. Wainwright, *CosmoTransitions: computing cosmological phase transition temperatures and bubble profiles with multiple fields*, *Comput. Phys. Commun.* **183** (2012) 2006 [arXiv:1109.4189] [ɪɴSPIRE].

[137] L. Fromme, S.J. Huber and M. Seniuch, *Baryogenesis in the two-Higgs doublet model*, *JHEP* **11** (2006) 038 [hep-ph/0605242] [INSPIRE].

[138] J.R. Espinosa and M. Quirós, *The electroweak phase transition with a singlet*, *Phys. Lett. B* **305** (1993) 98 [hep-ph/9301285] [INSPIRE].

[139] J.R. Espinosa and M. Quirós, *Novel effects in electroweak breaking from a hidden sector*, *Phys. Rev. D* **76** (2007) 076004 [hep-ph/0701145] [INSPIRE].

[140] S. Profumo, M.J. Ramsey-Musolf and G. Shaughnessy, *Singlet Higgs phenomenology and the electroweak phase transition*, *JHEP* **08** (2007) 010 [arXiv:0705.2425] [INSPIRE].

[141] J.R. Espinosa, T. Konstandin and F. Riva, *Strong electroweak phase transitions in the standard model with a singlet*, *Nucl. Phys. B* **854** (2012) 592 [arXiv:1107.5441] [INSPIRE].

[142] V. Barger, D.J.H. Chung, A.J. Long and L.-T. Wang, *Strongly first order phase transitions near an enhanced discrete symmetry point*, *Phys. Lett. B* **710** (2012) 1 [arXiv:1112.5460] [INSPIRE].

[143] D. Curtin, P. Meade and C.-T. Yu, *Testing electroweak baryogenesis with future colliders*, *JHEP* **11** (2014) 127 [arXiv:1409.0005] [INSPIRE].

[144] G. Kurup and M. Perelstein, *Dynamics of electroweak phase transition in singlet-scalar extension of the standard model*, *Phys. Rev. D* **96** (2017) 015036 [arXiv:1704.03381] [INSPIRE].

[145] M. Carena, Z. Liu and Y. Wang, *Electroweak phase transition with spontaneous Z_2-breaking*, *JHEP* **08** (2020) 107 [arXiv:1911.10206] [INSPIRE].

[146] J.M. Cline and K. Kainulainen, *Electroweak baryogenesis and dark matter from a singlet Higgs*, *JCAP* **01** (2013) 012 [arXiv:1210.4196] [INSPIRE].

[147] D.J.H. Chung and A.J. Long, *Cosmological constant, dark matter, and electroweak phase transition*, *Phys. Rev. D* **84** (2011) 103513 [arXiv:1108.5193] [INSPIRE].

[148] R. Cooke, M. Pettini, R.A. Jorgenson, M.T. Murphy and C.C. Steidel, *Precision measures of the primordial abundance of deuterium*, *Astrophys. J.* **781** (2014) 31 [arXiv:1308.3240] [INSPIRE].

[149] PLANCK collaboration, *Planck 2015 results. XIII. Cosmological parameters*, *Astron. Astrophys.* **594** (2016) A13 [arXiv:1502.01589] [INSPIRE].

[150] P.H. Damgaard, A. Haarr, D. O'Connell and A. Tranberg, *Effective field theory and electroweak baryogenesis in the singlet-extended standard model*, *JHEP* **02** (2016) 107 [arXiv:1512.01963] [INSPIRE].

[151] C. Balázs, G. White and J. Yue, *Effective field theory, electric dipole moments and electroweak baryogenesis*, *JHEP* **03** (2017) 030 [arXiv:1612.01270] [INSPIRE].

[152] J. de Vries, M. Postma, J. van de Vis and G. White, *Electroweak baryogenesis and the standard model effective field theory*, *JHEP* **01** (2018) 089 [arXiv:1710.04061] [INSPIRE].

[153] C. Grojean, G. Servant and J.D. Wells, *First-order electroweak phase transition in the standard model with a low cutoff*, *Phys. Rev. D* **71** (2005) 036001 [hep-ph/0407019] [INSPIRE].

[154] D. Bödeker, L. Fromme, S.J. Huber and M. Seniuch, *The baryon asymmetry in the standard model with a low cut-off*, *JHEP* **02** (2005) 026 [hep-ph/0412366] [INSPIRE].

[155] G.D. Moore, *Electroweak bubble wall friction: analytic results*, *JHEP* **03** (2000) 006 [hep-ph/0001274] [INSPIRE].

[156] S.J. Huber, M. Pospelov and A. Ritz, *Electric dipole moment constraints on minimal electroweak baryogenesis*, *Phys. Rev. D* **75** (2007) 036006 [hep-ph/0610003] [INSPIRE].

[157] M. Lewicki and V. Vaskonen, *Gravitational waves from colliding vacuum bubbles in gauge theories*, *Eur. Phys. J. C* **81** (2021) 437 [arXiv:2012.07826] [INSPIRE].

[158] A. Roper Pol, S. Mandal, A. Brandenburg, T. Kahniashvili and A. Kosowsky, *Numerical simulations of gravitational waves from early-universe turbulence*, *Phys. Rev. D* **102** (2020) 083512 [arXiv:1903.08585] [INSPIRE].

[159] T. Kahniashvili, A. Brandenburg, G. Gogoberidze, S. Mandal and A. Roper Pol, *Circular polarization of gravitational waves from early-Universe helical turbulence*, *Phys. Rev. Res.* **3** (2021) 013193 [arXiv:2011.05556] [INSPIRE].

[160] A. Roper Pol, S. Mandal, A. Brandenburg and T. Kahniashvili, *Polarization of gravitational waves from helical MHD turbulent sources*, arXiv:2107.05356 [INSPIRE].

[161] R. Jinno, T. Konstandin and H. Rubira, *A hybrid simulation of gravitational wave production in first-order phase transitions*, *JCAP* **04** (2021) 014 [arXiv:2010.00971] [INSPIRE].

[162] C. Gowling and M. Hindmarsh, *Observational prospects for phase transitions at LISA: Fisher matrix analysis*, *JCAP* **10** (2021) 039 [arXiv:2106.05984] [INSPIRE].

[163] M. Hindmarsh, S.J. Huber, K. Rummukainen and D.J. Weir, *Gravitational waves from the sound of a first order phase transition*, *Phys. Rev. Lett.* **112** (2014) 041301 [arXiv:1304.2433] [INSPIRE].

[164] H.-K. Guo, K. Sinha, D. Vagie and G. White, *Phase transitions in an expanding universe: stochastic gravitational waves in standard and non-standard histories*, *JCAP* **01** (2021) 001 [arXiv:2007.08537] [INSPIRE].

[165] LIGO SCIENTIFIC collaboration, *Advanced LIGO*, *Class. Quant. Grav.* **32** (2015) 074001 [arXiv:1411.4547] [INSPIRE].

[166] E. Thrane and J.D. Romano, *Sensitivity curves for searches for gravitational-wave backgrounds*, *Phys. Rev. D* **88** (2013) 124032 [arXiv:1310.5300] [INSPIRE].

[167] LIGO SCIENTIFIC, VIRGO collaboration, *GW150914: implications for the stochastic gravitational wave background from binary black holes*, *Phys. Rev. Lett.* **116** (2016) 131102 [arXiv:1602.03847] [INSPIRE].

[168] LIGO SCIENTIFIC, VIRGO collaboration, *Search for the isotropic stochastic background using data from Advanced LIGO's second observing run*, *Phys. Rev. D* **100** (2019) 061101 [arXiv:1903.02886] [INSPIRE].

[169] N. Bartolo et al., *Science with the space-based interferometer LISA. Part IV. Probing inflation with gravitational waves*, *JCAP* **12** (2016) 026 [arXiv:1610.06481] [INSPIRE].

[170] C. Caprini et al., *Reconstructing the spectral shape of a stochastic gravitational wave background with LISA*, *JCAP* **11** (2019) 017 [arXiv:1906.09244] [INSPIRE].

[171] M. Punturo et al., *The Einstein Telescope: a third-generation gravitational wave observatory*, *Class. Quant. Grav.* **27** (2010) 194002 [INSPIRE].

[172] S. Hild et al., *Sensitivity studies for third-generation gravitational wave observatories*, *Class. Quant. Grav.* **28** (2011) 094013 [arXiv:1012.0908] [INSPIRE].

[173] L. Badurina, O. Buchmueller, J. Ellis, M. Lewicki, C. McCabe and V. Vaskonen, *Prospective sensitivities of atom interferometers to gravitational waves and ultralight dark matter*, *Phil. Trans. A. Math. Phys. Eng. Sci.* **380** (2021) 20210060 [arXiv:2108.02468] [INSPIRE].

[174] AEDGE collaboration, *AEDGE: Atomic Experiment for Dark matter and Gravity Exploration in space*, *EPJ Quant. Technol.* **7** (2020) 6 [`arXiv:1908.00802`] [InSPIRE].

[175] L. Badurina et al., *AION: an Atom Interferometer Observatory and Network*, *JCAP* **05** (2020) 011 [`arXiv:1911.11755`] [InSPIRE].

[176] E.J. Weinberg, *Radiative corrections as the origin of spontaneous symmetry breaking*, Ph.D. thesis, Harvard University, U.S.A. (1973), `hep-th/0507214` [InSPIRE].

[177] C. Delaunay, C. Grojean and J.D. Wells, *Dynamics of non-renormalizable electroweak symmetry breaking*, *JHEP* **04** (2008) 029 [`arXiv:0711.2511`] [InSPIRE].

[178] J. Elias-Miro, J.R. Espinosa and T. Konstandin, *Taming infrared divergences in the effective potential*, *JHEP* **08** (2014) 034 [`arXiv:1406.2652`] [InSPIRE].

[179] S.P. Martin, *Taming the Goldstone contributions to the effective potential*, *Phys. Rev. D* **90** (2014) 016013 [`arXiv:1406.2355`] [InSPIRE].

[180] A. Linde, *Infrared problem in the thermodynamics of the Yang-Mills gas*, *Phys. Lett. B* **96** (1980) 289.

[181] P.M. Schicho, T.V.I. Tenkanen and J. Österman, *Robust approach to thermal resummation: standard model meets a singlet*, *JHEP* **06** (2021) 130 [`arXiv:2102.11145`] [InSPIRE].

[182] L. Niemi, P. Schicho and T.V.I. Tenkanen, *Singlet-assisted electroweak phase transition at two loops*, *Phys. Rev. D* **103** (2021) 115035 [`arXiv:2103.07467`] [InSPIRE].

[183] S. Weinberg, *Gauge and global symmetries at high temperature*, *Phys. Rev. D* **9** (1974) 3357 [InSPIRE].

[184] P.B. Arnold and O. Espinosa, *The effective potential and first order phase transitions: Beyond leading-order*, *Phys. Rev. D* **47** (1993) 3546 [*Erratum ibid.* **50** (1994) 6662] [`hep-ph/9212235`] [InSPIRE].

[185] D. Curtin, P. Meade and H. Ramani, *Thermal resummation and phase transitions*, *Eur. Phys. J. C* **78** (2018) 787 [`arXiv:1612.00466`] [InSPIRE].